Small-Signal Modeling of *LLC* Converters Using Homopolarity Cycle

Mehdi Mohammadi, *Student Member, IEEE*, Franco Degioanni, *Student Member, IEEE*, Mohammad Mahdavi, and Martin Ordonez, *Member, IEEE*

***Abstract*—The widespread use of the *LLC* converter in dc–dc applications has increased the importance of small-signal modeling to control the converter below- to above-resonant frequency. The analysis of *LLC* converters is complicated, since they process the electrical energy through a high-frequency resonant tank that causes excessive nonlinearity. As a result of this complexity, small-signal modeling of the *LLC* converter is traditionally performed using empirical methods, iterative simulation approaches, or theory limited to the vicinity of the resonant frequency. Often, such approaches may lead to limited insight (just empirical trends) or low accuracy below and above resonance. This article proposes a new average small-signal modeling technique for the *LLC* converter, and it is performed in the time domain. The proposed technique is based on the analysis of the homopolarity cycle and accurately predicts not only the small-signal dynamic behavior of the *LLC* converter at resonance, but also below and above resonance. By using the homopolarity cycle, the theoretical analysis of the *LLC* converter is significantly simplified to a level that the small-signal dynamic behavior of the *LLC* converter is expressed by two second-order circuit models. Experimental and simulation results of a 650-W *LLC* converter are provided to verify the theoretical analyses and accuracy of the circuit models. The results have shown that the proposed small-signal circuit models can accurately predict the small-signal dynamic behaviors of the *LLC* converter from below- to above-resonant operations.**

***Index Terms*—Behavioral analysis, homopolarity cycle, *LLC*, small-signal model.**

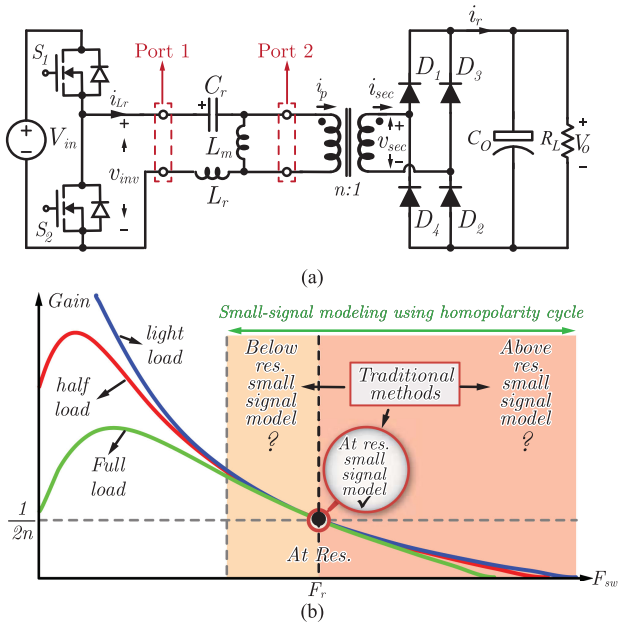

Fig. 1. (a) Circuit schematic of the half-bridge *LLC* converter. (b) Gain-frequency diagram, illustrating that the *LLC* converter can operate in three regions, and that most of the traditional small-signal modeling techniques are performed in the vicinity of the resonant frequency.

I. Introduction

THE insistence on gaining higher efficiency and power density and reduced electromagnetic interference has caused *LLC* converters to achieve popularity in dc–dc power conversion applications, such as battery chargers for electric vehicles, fuel cell and solar panel energy systems, and LED drivers [1]–[4]. As shown in Fig. 1(a), *LLC* converters transfer energy through a high-frequency resonant tank, behaving as a bandpass filter. The components of the resonant tank have zero mean voltage and current values in a switching cycle, and therefore, unlike pulsewidth modulation converters, traditional averaging techniques cannot be directly used for small-signal modeling of *LLC* converters [6]. Therefore, more complicated techniques are required for the analysis and modeling of *LLC* converters [5].

Generally, the first step in obtaining the small-signal model of *LLC* converters is the analysis of their large-signal dynamic behavior. The large-signal dynamic behavior of *LLC* converters can be expressed through a set of nonlinear discrete state-space equations [7]. Discrete state-space equations are nonlinear, and they must be linearized first before they are used for small-signal modeling. Linearization of the discrete state-space equations can be conventionally performed either by Taylor or Fourier expansion around the equilibrium point and most of times in the vicinity of the resonant frequency [8]–[20]. Usually, linearization through the Taylor expansion produces high-order equations, and this makes the derivation of the analytical small-signal transfer function complicated [8]–[13]. Therefore, empirical/numerical methods are commonly employed to obtain the

Manuscript received December 5, 2018; revised March 4, 2019 and May 19, 2019; accepted July 24, 2019. Date of publication August 4, 2019; date of current version January 10, 2020. This work was supported by the Natural Sciences and Engineering Research Council, Canada. Recommended for publication by Associate Editor P. Mattavelli. *(Corresponding author: Mehdi Mohammadi.)*

M. Mohammadi is with Fortinet Technologies, Burnaby, BC V5C 6C6, Canada (e-mail: mehdi.mohammadi.m@ieee.org).

F. Degioanni, M. Mahdavi, and M. Ordonez are with the Department of Electrical and Computer Engineering, The University of British Columbia, Vancouver, BC V6T 1Z4, Canada (e-mail: fdegioanni@ieee.org; mahdavi@ece.ubc.ca; mordonez@ieee.org).

Color versions of one or more of the figures in this article are available online at http://ieeexplore.ieee.org.

Digital Object Identifier 10.1109/TPEL.2019.2933179

small-signal transfer function [13]. Extended describing function (EDF) small-signal modeling techniques, on the other side, linearize the nonlinear state-space equations using the Fourier expansion [14]–[20]. In EDF methods, the Fourier expansion can be performed by considering only the first harmonic; however, if a higher accuracy is needed, higher order harmonics can be taken into consideration. Traditional EDF techniques usually result in high-order transfer functions, which are represented by a set of matrices rather than an equivalent circuit. In more advanced EDF techniques, the small-signal transfer function is simplified and represented by an equivalent circuit [21], [22]. This is enabled by the analysis of signal envelopes.

Small-signal modeling of *LLC* converters can also be performed using the communication theory [23]. In this method, the effects of the first, third, and seventh harmonics on the dynamic behavior of the *LLC* converter are separately analyzed, and then, their effects are superposed. In some applications, the switching frequency of *LLC* converters is kept fixed, and the voltage regulation is obtained by a switched capacitor. In this type of *LLC* converters, the amplitude modulation technique, which is based on analyzing the dynamic behavior of the switched capacitor, has to be used for extracting the small-signal model [24]. In the frequency domain, the load can be modeled as a time-varying resistor. The magnitude and phase of the time-varying resistor are obtained through an iterative procedure and require empirical implementation. Based on the time-varying resistor model, the small-signal transfer function using conversion matrix techniques can be obtained [25]. Another small-signal modeling technique, addressed in the literature, is performed through the obtainment of the lumped parameter equivalent circuit, describing the linearized behavior of switched tank elements [26]. Recently, time-domain low-frequency modeling of resonant converters, including *LLC* and series-resonant converters, operating at resonance, has been reported in literature [27]–[30]. Besides the fact that simplification is achieved via the time-domain analysis, the models obtained are accurate when the *LLC* converter operates at resonance. Therefore, the accuracy of the models degrade below and above resonance.

As shown in Fig. 1(b), *LLC* converters are required to operate below, at, and above resonance in order to provide voltage regulation. As discussed, most of the current small-signal modeling techniques for *LLC* converters are mainly based on empirical approaches or performed in the vicinity of the resonant frequency (F_r). As a result, the accuracy of those models degrades when the switching frequency (F_{sw}) as the control signal is not equal to the resonant frequency. Therefore, the opportunity to introduce a new analytical time-domain small-signal modeling technique, which is accurate below, at, and above resonance and reduces the complexity of the analysis, is still open.

This article proposes a new small-signal modeling technique for *LLC* converters, which is based on the analysis of the homopolarity cycle in the time domain. As shown in Fig. 1(b), unlike most of the traditional techniques, which model the dynamic behavior of the *LLC* converter around the resonance, the proposed technique accurately models the small-signal dynamic behavior of the *LLC* converter not only at resonance, but also below and above resonance, while reducing the complexity

	Homopolairty cycle	FHA based	Empirical based
Derivation	Simple	Complex	-
Order of the model	2nd	>=3rd	-
Analysis domain	Time-domain	Time+freq. domain	-
Circuit Represention	Yes simple	Sometimes complicated	No
Validity range	Below to above resonance	Around resonance	At one operating point
Accuracy	High in the entire range of Fsw	Good around the resonant freq.	High at each operating point

Fig. 2. Comparison of properties: the proposed, first harmonic approximation, and empirical-based small-signal modeling techniques.

of the analysis. The below-, at-, and above-resonant dynamic behaviors are represented by two second-order circuit models, and no simulation, numerical computing, or programming software packages are required to analyze the proposed models and obtain their transfer functions. The circuit representation is an advantage as it helps designers/engineers to more effectively understand the small-signal nature of the *LLC* converter. To highlight the advantages of the proposed small-signal modeling technique, in Fig. 2, it is conceptually compared with the traditional small-signal modeling techniques. The homopolarity cycle mathematically explains the relationship between the polarities of the inverter voltage v_{inv} and secondary voltage/current (v_{sec} or i_{sec}) and will be discussed in detail in Section II. The theoretical analyses are validated through experimental and simulation results of a 650-W *LLC* converter. The results have shown that the proposed second-order circuit models predict the small-signal dynamic behavior of the *LLC* converter with high accuracy from below- to above-resonant operations.

II. Voltage Gain, Homopolarity Cycle, and Switching Frequency Relationship

In order to address the complexity and accuracy concerns when deriving the small-signal model of the *LLC* converter in all operating regions (i.e., below, at, and above resonance), the homopolarity cycle can be introduced to time-domain equations of the *LLC* converter. The homopolarity cycle describes the volt–amp–second balance principle and simplifies the theoretical analysis in such a way that two second-order circuit models are obtained to illustrate the small-signal dynamic behavior of the *LLC* converter.

In this section, the dc voltage gain of the *LLC* converter as a function of the homopolarity cycle and switching frequency is obtained. The homopolarity cycle is defined as follows: the ratio of a period of time during which the polarities of the inverter voltage and v_{sec} or i_{sec} are the same to half a switching period. The resonant tank of the *LLC* converter is made of two inductors and one capacitor. In the steady state, the volt–second and amp–second balance conditions are satisfied for the resonant inductors and capacitor, respectively. Therefore, if the resonant tank is considered as a component with two terminals, the volt–amp–second balance condition is satisfied for the resonant tank, in the

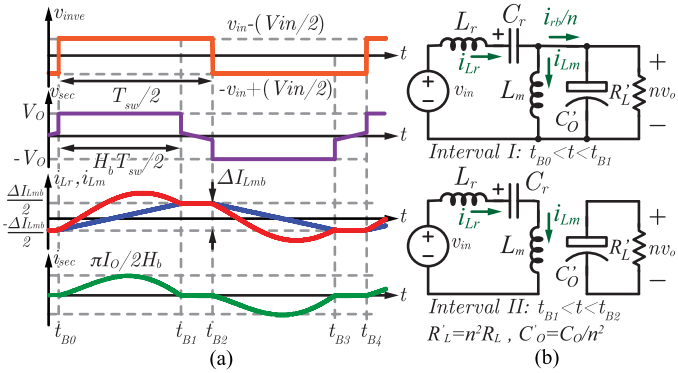

Fig. 3. Half-bridge *LLC* converter. (a) Key time-domain waveforms below resonance. (b) Corresponding circuit schematics to the first two operating intervals.

steady state. The homopolarity cycle mathematically explains the volt–amp–second balance principle in *LLC* converters.

The analysis performed in this article is mainly focused on the half-bridge *LLC* converter; however, it can be easily extended to the full-bridge *LLC* converter. In the steady state, the resonant capacitor of the *LLC* converter has a dc voltage offset of $V_{\text{in}}/2$. The analysis of the *LLC* converter in the time domain requires understanding the operating intervals. Design of the *LLC* converter and time-domain analysis of intervals are already discussed in literature [31], [32]. Therefore, by knowing that the fundamental concepts of designing and analyzing the time-domain intervals are already available, this article mainly focuses on small-signal modeling for the *LLC* converter in the time domain.

In order to analyze the *LLC* converter steady-state operation, the following assumptions are taken into consideration.

1) All the parasitic elements are negligible.
2) All the components are ideal.
3) The below-resonant magnetizing current variation in Interval II is very small and can be neglected.

In order to more effectively explain the derivation of the dc voltage gain for each operating region, this section is divided into three subsections.

A. Voltage Gain Below Resonance

The *LLC* converter, working below resonance, has four operating intervals in a switching cycle. Since the operation of the *LLC* converter is symmetrical in a switching cycle, the analysis of the first two operating intervals suffices. The key time-domain waveforms and circuit schematics corresponding to the first two operating intervals of the *LLC* converter, operating below resonance, are shown in Fig. 3. As shown in this figure, from t_{B0} to t_{B1}, $v_{\text{inv}} - (V_{\text{in}}/2)$ and v_{sec} or i_{sec} have the same polarity (both are positive). When the *LLC* converter operates below resonance, the homopolarity cycle is defined as follows:

$$H_b := \frac{t_{B1} - t_{B0}}{T_{\text{sw}}/2} \tag{1}$$

where T_{sw} is the switching period.

The circuit schematic corresponding to the below-resonant operation of the *LLC* converter in Interval I is shown in Fig. 3(b). The differential equation expressing the below-resonant operation of the *LLC* converter in Interval I is given as follows:

$$V_{\text{in}} - nV_O = L_r \frac{di_{Lr}(t)}{dt} + v_{Cr}(t). \tag{2}$$

Integrating (2) from t_{B0} to t_{B1} results in the following equation:

$$(V_{\text{in}} - nV_O)H_b\frac{T_{\text{sw}}}{2} = L_r[i_{Lr}(t_{B1}) - i_{Lr}(t_{B0})] + \int_{t_{B0}}^{t_{B1}} v_{Cr}(t)dt. \tag{3}$$

The circuit schematic corresponding to the below-resonant operation of the *LLC* converter in Interval II is shown in Fig. 3(b). The differential equation expressing the below-resonant operation of the *LLC* converter in Interval II is given as follows:

$$V_{\text{in}} = L_r \frac{di_{Lr}(t)}{dt} + v_{Cr}(t) + L_m \frac{di_{Lm}(t)}{dt}. \tag{4}$$

Integrating (4) from t_{B1} to t_{B2} results in the following equation:

$$V_{\text{in}}(1 - H_b)\frac{T_{\text{sw}}}{2} = L_r[i_{Lr}(t_{B2}) - i_{Lr}(t_{B1})] + \int_{t_{B1}}^{t_{B2}} v_{Cr}(t)dt + L_m[i_{Lm}(t_{B2}) - i_{Lm}(t_{B1})]. \tag{5}$$

The resonant current is periodic. Therefore, $i_{Lr}(t_{B2}) = -i_{Lr}(t_{B0})$ and $i_{Lr}(t_{B2}) - i_{Lr}(t_{B0}) = \Delta I_{\text{Lmb}}$. Also, $i_{Lr}(t_{B2}) \approx i_{Lr}(t_{B1})$. Therefore, adding (3) to (5) results in the following equation:

$$(V_{\text{in}} - nV_O)H_b\frac{T_{\text{sw}}}{2} + V_{\text{in}}(1 - H_b)\frac{T_{\text{sw}}}{2} = L_r\Delta I_{Lmb} + \int_{t_{B0}}^{t_{B2}} v_{Cr}(t)dt. \tag{6}$$

From t_{B0} to t_{B1}, nV_O drops across L_m and linearly increases i_{Lm}. In this time period, i_{Lm} can be calculated using the following equation:

$$i_{Lm}(t) = \frac{nV_O}{L_m}(t - t_{B0}) - \frac{\Delta I_{Lmb}}{2} \quad (t_{B0} < t < t_{B1}). \tag{7}$$

Below resonance, $t_{B1} - t_{B0} = T_r/2$. T_r is the series-resonant period and can be calculated using $2\pi\sqrt{L_rC_r}$. Therefore, ΔI_{Lmb} can be obtained using the following equation:

$$\Delta I_{Lmb} = \frac{nV_OT_r}{2L_m}. \tag{8}$$

Below resonance, $L_r\Delta I_{Lmb} + \int_{t_{B0}}^{t_{B2}} v_{Cr}(t)dt \approx (V_{\text{in}}T_{\text{sw}})/4$. Therefore, (6) can be rewritten as follows:

$$(V_{\text{in}} - nV_O)H_b\frac{T_{\text{sw}}}{2} + V_{\text{in}}(1 - H_b)\frac{T_{\text{sw}}}{2} = \frac{V_{\text{in}}}{2}\frac{T_{\text{sw}}}{2}. \tag{9}$$

Manipulating the above equation results in an equation expressing the dc voltage gain of the *LLC* converter operating

below resonance as a function of H_b

$$\frac{V_O}{V_{\text{in}}} = \frac{1}{2nH_b}. \tag{10}$$

According to Fig. 3(a), the conduction time period of the rectifier in half a switching cycle equals $H_bT_{\text{sw}}/2$. This conduction time when the *LLC* converter operates below resonance is half a series-resonant period ($T_r/2$). Therefore, $(H_bT_{\text{sw}})/2 = T_r/2$. The ratio of the series-resonant frequency F_r to the switching frequency F_{sw} is called K_f and is defined as follows:

$$K_f := \frac{F_r}{F_{\text{sw}}} = \frac{T_{\text{sw}}}{T_r}. \tag{11}$$

By applying (11) to (10), the relationship between the below-resonant voltage gain, homopolarity cycle, and switching frequency is obtained as

$$\frac{V_O}{V_{\text{in}}} = \frac{1}{2nH_b} = \frac{K_f}{2n}. \tag{12}$$

In the following, the conditions under which the below-resonant voltage gain equation given by (12) remains accurate is discussed. While deriving the below-resonant voltage gain equation of the *LLC* converter, it was assumed that the variation in the magnetizing current is negligible in Interval II, and that the converter has four operating intervals in a switching cycle. To guarantee that the variation in the magnetizing current in Interval II is negligible, the resonant period (T_{rb}) of the resonance occurred in Interval II in the below-resonant operation must be much larger than the largest period that the *LLC* converter remains in Interval II. Below resonance, from t_{B1} to t_{B2}, the *LLC* converter is in Interval II. According to the above discussion, $t_{B2} - t_{B1} = (1 - H_b)(T_{\text{sw}}/2)$. The largest period within which the *LLC* converter operates below resonance in Interval II happens when the *LLC* converter is required to produce the largest voltage gain. According to (12), the largest voltage gain is achieved when the switching frequency is minimum. If the switching frequency is minimum, the below-resonant homopolarity cycle H_b is minimum as well. The minimum below-resonant homopolarity cycle $H_{b-\text{min}}$ can be calculated by using the following equation:

$$H_{b-\text{min}} = \frac{F_{\text{sw-min}}}{F_r}. \tag{13}$$

The resonant period of the resonance that occurs in Interval II in the below-resonant operation can be calculated through the following equation:

$$T_{rb} = 2\pi\sqrt{(L_r + L_m)C_r}. \tag{14}$$

In order to guarantee the accuracy of the below-resonant voltage gain, even at the minimum switching frequency, the following condition must be satisfied:

$$(1 - H_{b-\text{min}})\frac{1}{2F_{\text{sw-min}}} << 2\pi\sqrt{(L_r + L_m)C_r}. \tag{15}$$

As illustrated in Fig. 1(b), as long as the above condition is satisfied, and the quality factor Q is smaller than Q_{max} (full instructions to calculate Q_{max} is provided in [32]), in the below-resonant operation, from $F_{\text{sw-min}}$ to F_r, the voltage gain curves converge to each other, and this is expressed by the proposed below-resonant voltage gain equation given by (12). If the above conditions are satisfied, this phenomenon can also be seen in other works, such as the one presented in [33].

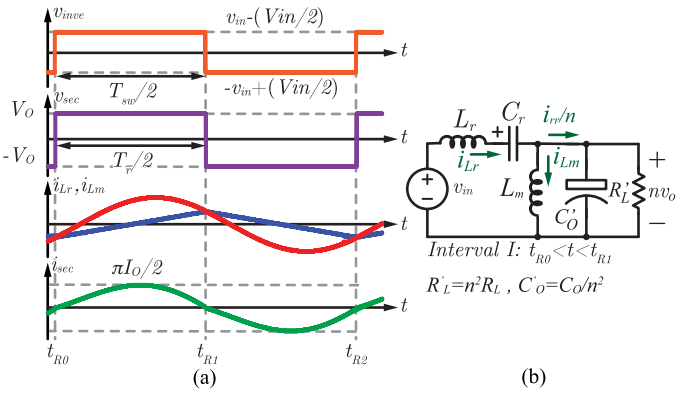

Fig. 4. Half-bridge *LLC* converter. (a) Key time-domain waveforms at resonance. (b) Corresponding circuit schematic of the first operating interval at resonance.

B. Voltage Gain at Resonance

The *LLC* converter, working at resonance, has two operating intervals in a switching cycle. Since the operation of the *LLC* converter is symmetrical in a switching cycle, the analysis of the first operating interval suffices. The key time-domain waveforms and circuit schematic corresponding to the first operating interval of the *LLC* converter, at resonance, are shown in Fig. 4. As shown in this figure, from t_{R0} to t_{R1}, $v_{\text{inv}} - (V_{\text{in}}/2)$ and v_{sec} or i_{sec} have the same polarity (both are positive). Since $t_{R1} - t_{R0} = T_{\text{sw}}/2$, the homopolarity cycle equals 1 when the *LLC* converter operates at resonance.

The circuit schematic corresponding to the *LLC* converter, operating at resonance and in Interval I, is shown in Fig. 4(b). The differential equation expressing the resonant operation of the *LLC* converter in Interval I is given as by (2). Integrating (2) from t_{R0} to t_{R1} results in the following equation:

$$(V_{\text{in}} - nV_O)\frac{T_{\text{sw}}}{2} = L_r[i_{Lr}(t_{R1}) - i_{Lr}(t_{R0})] + \int_{t_{R0}}^{t_{R1}} v_{Cr}(t)dt. \tag{16}$$

Since $L_r[i_{Lr}(t_{R1}) - i_{Lr}(t_{R0})] = nV_O(L_r/L_m)(T_{\text{sw}}/2)$, $\int_{t_{R0}}^{t_{R1}} v_{Cr}(t)dt = \{(V_{in}/2) - [nV_O(L_r/L_m)]\}(T_{\text{sw}}/2)$, and $L_r < L_m$, (16) can be simplified as follows:

$$(V_{\text{in}} - nV_O)\frac{T_{\text{sw}}}{2} = \frac{V_{\text{in}}}{2}\frac{T_{\text{sw}}}{2}. \tag{17}$$

Manipulating the above equation results in an equation, expressing the dc voltage gain of the *LLC* converter, operating at resonance

$$\frac{V_O}{V_{\text{in}}} = \frac{1}{2n}. \tag{18}$$

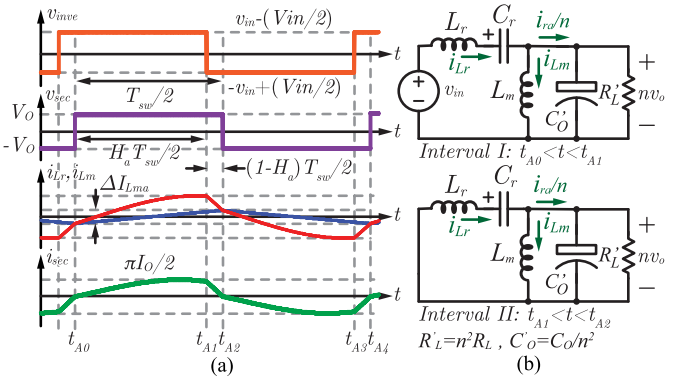

Fig. 5. Half-bridge *LLC* converter. (a) Key time-domain waveforms above resonance. (b) Circuit schematics corresponding to the first half cycle in the above-resonant operation.

C. Voltage Gain Above Resonance

The *LLC* converter, working above resonance, has four operating intervals in a switching cycle. Since the operation of the *LLC* converter is symmetrical in a switching cycle, the analysis of the first two operating intervals suffices. The key time-domain waveforms and circuit schematics corresponding to the first two operating intervals of the *LLC* converter, operating above resonance, are shown in Fig. 5. As shown in this figure, from t_{A0} to t_{A1}, $v_{\text{inv}} - (V_{\text{in}}/2)$ and v_{sec} or i_{sec} have the same polarity (both are positive). When the *LLC* converter operates above resonance, the homopolarity cycle is defined as follows:

$$H_a := \frac{t_{A1} - t_{A0}}{T_{\text{sw}}/2}. \tag{19}$$

The circuit schematic corresponding to the above-resonant operation of the *LLC* converter in Interval I is shown in Fig. 5(b). The differential equation expressing the operation of the *LLC* converter in Interval I is given by (2). Integrating (2) from t_{A0} to t_{A1} results in the following equation:

$$(V_{\text{in}} - nV_O)H_a\frac{T_{\text{sw}}}{2} = L_r[i_{Lr}(t_{A1}) - i_{Lr}(t_{A0})] + \int_{t_{A0}}^{t_{A1}} v_{Cr}(t)dt. \tag{20}$$

The corresponding circuit schematic to the above-resonant operation of the *LLC* converter in Interval II is shown in Fig. 5(b). The differential equation expressing the operation of the *LLC* converter in Interval II is given as follows:

$$-nV_O = L_r\frac{di_{Lr}(t)}{dt} + v_{Cr}(t). \tag{21}$$

Integration the above equation from t_{A1} to t_{A2} results in the following equation:

$$-nV_O(1-H_a)\frac{T_{\text{sw}}}{2} = L_r[i_{Lr}(t_{A2}) - i_{Lr}(t_{A1})] + \int_{t_{A1}}^{t_{A2}} v_{Cr}(t)dt. \tag{22}$$

Adding (20) to (22) results in the following equation:

$$(V_{\text{in}} - nV_O)H_a\frac{T_{\text{sw}}}{2} - nV_O(1-H_a)\frac{T_{\text{sw}}}{2} = L_r\Delta I_{Lma} + \int_{t_{A0}}^{t_{A2}} v_{Cr}(t)dt \tag{23}$$

where $\Delta I_{Lma} = (nV_OT_{\text{sw}})/2L_m$ and $(2/T_{\text{sw}})\int_{t_{A0}}^{t_{A2}} v_{Cr}(t)dt = 0.5V_{\text{in}} + V_O[(1/K_f) - 1]/[8nF_{\text{sw}}C_rR_L] - L_r(nV_OT_{\text{sw}})/2L_m$. Therefore, (23) can be rewritten as follows:

$$(V_{\text{in}} - nV_O)H_a\frac{T_{\text{sw}}}{2} - nV_O(1-H_a)\frac{T_{\text{sw}}}{2} = \left\{\frac{V_{\text{in}}}{2} + \frac{V_O[(1/K_f)-1]}{8nF_{\text{sw}}C_rR_L}\right\}\frac{T_{\text{sw}}}{2}. \tag{24}$$

Manipulating (24) results in the following equation, expressing the dc voltage gain of the *LLC* converter operating above resonance:

$$\frac{V_O}{V_{\text{in}}} = \frac{H_a - 0.5}{n + \frac{(1/K_f)-1}{8nF_{\text{sw}}C_rR_L}}. \tag{25}$$

The above equation shows that the voltage gain of the *LLC* converter depends not only on the switching frequency (the control signal), but also on the above-resonant homopolarity cycle H_a and load. Since H_a is indeed a consequence and cannot be controlled directly, it has to be calculated. To calculate the output voltage or voltage gain, the input voltage, load, and switching frequency are considered as known parameters. The unknowns are H_a and V_O. To compute the unknowns, in addition to (25), another equation as a function of the same unknowns is required.

Ideally, it can be said that $P_O = P_{\text{in}}$, where P_O and P_{in} are the output and input powers, respectively. As a result, the following equation can be written as:

$$\frac{V_O}{V_{\text{in}}} = \frac{I_{\text{in}}}{I_O} \tag{26}$$

where I_{in} and I_O are the average input and output currents, respectively.

As illustrated in Fig. 5, the input voltage is connected to the circuit in Interval I, and in this interval, the input current equals the current through the resonant inductor i_{Lr}. I_{in} can be calculated through the following equation:

$$I_{\text{in}} = \frac{1}{T_{\text{sw}}}\int_{t_{A0}}^{t_{A1}} i_{Lr}dt = \frac{1}{T_{\text{sw}}}\int_{t_{A0}}^{t_{A1}} \frac{1}{n}i_{ra}dt + \int_{t_{A0}}^{t_{A1}} i_{Lm}dt. \tag{27}$$

From t_{A0} to t_{A1}, $i_{Lm}(t) = (nV_O/L_m)(t - t_{A0}) - (\Delta I_{Lma}/2)$. As discussed later in this article, $\Delta I_{Lma} = nV_O/2L_mF_{\text{sw}}$.

According to the discussion made in Section III-B and Fig. 8, above resonance and in Interval I, $i_{ra} = I_{pa}\sin(\omega_r t)$. I_{pa} is given by (60). By solving (27), the following equation is obtained:

$$I_{\text{in}} = \frac{I_{pa}}{2\pi nK_f}[1 - \cos(\pi K_f H_a)] + \frac{nV_OH_a(H_a-1)}{4L_mF_{\text{sw}}}. \tag{28}$$

By applying (28) and (60) to (26), and considering that $V_O/I_O = R_L$, the following equation is obtained:

$$\frac{V_O}{V_{\text{in}}} = \frac{1-\cos(\pi K_f H_a)}{2n[1-\cos(\pi K_f H_a)] + 0.5(1-H_a)\sin(\pi K_f H_a)} + \frac{nR_L H_a(H_a-1)}{4L_m F_{\text{sw}}}. \tag{29}$$

By using (29) and (25), the *LLC* converter voltage gain and H_a can be calculated.

Equations (12), (18), and (25) can all be unified in one equation. In general, the dc voltage gain of the *LLC* converter, homopolarity cycle, and switching frequency can all be calculated using the following equation:

$$\frac{V_O}{V_{\text{in}}} = \begin{cases} \frac{1}{2nH_b} = \frac{K_f}{2n}, & f_{\text{sw}} < f_0 \\ \frac{1}{2n}, & f_{\text{sw}} = f_0 \\ \frac{H_a - 0.5}{n + \frac{(1/K_f)-1}{8nF_{\text{sw}}C_r R_L}}, & f_{\text{sw}} > f_0. \end{cases} \tag{30}$$

III. Behavioral Average Equivalent Circuit: First Stage

In order to accurately predict the small-signal dynamic behavior of the *LLC* converter from below to above-resonant operations, and to reduce the complexity of the analysis, the homopolarity cycle was introduced in Section II. As it will be discussed in the following, by using the homopolarity cycle, the theoretical analysis is simplified to a level that the small-signal dynamic behavior of the *LLC* converter can be expressed by two second-order circuit models.

Now that the homopolarity cycle is defined, and the dc voltage gain, switching frequency, and homopolarity cycle relationships are formulated, the process of extracting the average small-signal model (ASSM) of the *LLC* converter can be started. The process of obtaining the ASSM of the *LLC* converter, using the homopolarity cycle concept, has three stages. The first two stages are involved in the obtainment of two behavioral average equivalent circuits. In the third stage, small-signal perturbations are applied to the signals of the *LLC* converter in order to theoretically obtain the small-signal model of the *LLC* converter. In this section, the focus of the analysis is on the first stage, in which the order of the *LLC* converter is reduced to three from four using the behavioral averaging technique, enabled by the homopolarity cycle concept.

A. Below-Resonant Third-Order Behavioral Average Equivalent Circuit

The small-signal model of the *LLC* converter can be obtained by average behavioral modeling of the elements. In this section, the first element that is behaviorally modeled is the magnetizing inductor L_m. The behavioral modeling of the magnetizing inductor requires discussion on its below-resonant voltage and current waveforms. The process of modeling L_m is based on obtaining the average values of the magnetizing voltage and current in half a switching cycle. As it will be discussed later in this section, in half a switching cycle, the average current through L_m is a function of nV_O, and nV_O is indeed the average voltage over L_m in half a switching cycle. Therefore, below resonance and in half a switching cycle, it can be concluded that L_m behaves similar to a voltage-dependent current source, on average. Since the current of the voltage-dependent current source depends on its average voltage, it can be simply modeled by a resistor.

If it is considered that the *LLC* converter is operating in the steady state and below resonance, as shown in Fig. 3(a), nV_O drops across the magnetizing inductor L_m from t_{B0} to t_{B1} and causes i_{Lm} to linearly increase. In interval I ($t_{B0} < t < t_{B1}$), i_{Lm} can be calculated using (7). According to this equation, $i_{Lm}(t_{B0}) = -\Delta I_{Lmb}/2$. In Section II, it was discussed that $t_{B1} - t_{B0} = H_b(T_{sw}/2) = T_r/2$. Therefore, at $t = t_{B1}$, the current through the magnetizing inductor becomes $\Delta I_{Lmb}/2$. This means that $i_{Lm}(t_{B1}) - i_{Lm}(t_{B0}) = \Delta I_{Lmb}$. ΔI_{Lmb} is already calculated using (8).

In Interval II, as shown in Fig. 3(a), the variation in the magnetizing current (di_{Lm}/dt) is almost zero. This means that from t_{B1} to t_{B2}, the amplitude of i_{Lm} remains almost constant at $\Delta I_{Lmb}/2$. The average current through the magnetizing inductor in half a switching period can be calculated using the following equation:

$$i_{Lm-\text{avg}} = \frac{2}{T_{\text{sw}}}\left\{\int_{t_{B0}}^{t_{B1}}\left[\frac{nV_O}{L_m}(t-t_{B0}) - \frac{\Delta I_{Lmb}}{2}\right]dt + \int_{t_{B1}}^{t_{B2}}\frac{\Delta I_{Lmb}}{2}dt\right\}. \tag{31}$$

In the above equation, $\int_{t_{B0}}^{t_{B1}}[(nV_O/L_m)(t-t_{B0}) - (\Delta I_{Lmb}/2]dt = 0$. Since $t_{B2} - t_{B1} = (1-H_b)(T_{\text{sw}}/2)$, (31) results in the following equation:

$$i_{Lm-\text{avg}} = \frac{nV_O(1-H_b)}{4L_m F_r}. \tag{32}$$

Below resonance and in Interval I, nV_O drops across L_m. In Interval II, $di_{Lm}/dt \approx 0$. Therefore, the average voltage over L_m in half a switching cycle from t_{B0} to t_{B2} equals $H_b nV_O$. By dividing the average voltage of the magnetizing inductor by its average current, L_m can be modeled by a resistor whose resistance is given by the following equation:

$$R_{Lmb} = \frac{4H_b L_m F_r}{1-H_b}. \tag{33}$$

According to (12), $H_b = 1/K_f$. Therefore, another way to write (33) is given as follows:

$$R_{Lmb} = \frac{4L_m F_r}{K_f - 1}. \tag{34}$$

The latter form to mathematically express R_{Lmb} is more appropriate because the actual control signal in the *LLC* converter is the switching frequency, and $K_f = F_r/F_{\text{sw}}$.

The differential equation, describing the below-resonant behavior of the *LLC* converter in Interval I, is given by (2). The below-resonant rectifier current, i_{rb}, in Interval I can be calculated using the following equation:

$$i_{rb} = n(i_{Lr} - i_{Lm}). \tag{35}$$

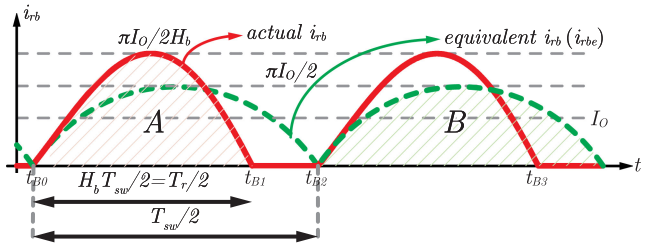

Fig. 6. Actual and equivalent rectifier current of the *LLC* converter, operating below resonance.

By applying (35) to (2), the following differential equation is obtained:

$$V_{\text{in}} - nV_O = \frac{L_r}{n}\frac{di_{rb}(t)}{dt} + L_r\frac{di_{Lm}(t)}{dt} + \frac{1}{nC_r}\int_{t_{B0}}^{t} i_{rb}(t)dt + \frac{1}{C_r} \times \int_{t_{B0}}^{t} i_{Lm}(t)dt + v_{Cr}(t_{B0}). \tag{36}$$

In Interval I, nV_O drops across L_m. Therefore, we have

$$\frac{di_{Lm}(t)}{dt} = \frac{nV_O}{L_m}. \tag{37}$$

By applying (37) to (36), the following differential equation is obtained:

$$\frac{d^4i_r(t)}{dt^4} + \frac{1}{L_rC_r}\frac{d^2i_r(t)}{dt^2} = 0. \tag{38}$$

The characteristic equation of the above differential equation is $S^4 + [1/(L_rC_r)]S^2 = 0$. The roots associated with the characteristic equation are 0 and $\pm j1/\sqrt{L_rC_r}$. Therefore, i_{rb}, below resonance and in Interval I, can be mathematically expressed in the time domain as follows:

$$i_{rb}(t) = \frac{1}{n} \times \frac{V_{\text{in}} - v_{Cr}(t_{B0}) - [1 + (L_r/L_m)]nV_O}{Z_r}\sin(\omega_r(t - t_{B0})) \tag{39}$$

where

$$\omega_r = \frac{1}{\sqrt{L_rC_r}} \tag{40}$$

$$Z_r = \sqrt{\frac{L_r}{C_r}}. \tag{41}$$

From t_{B1} to t_{B2}, $i_{rb} = 0$. The waveform of the below-resonant rectifier current is shown in Fig. 6 in red. In the steady state, the load current I_O equals the mean value of i_{rb}. Therefore, the pick current of i_{rb} can be simply calculated as $\pi I_O/(2H_b)$. This simply states that the coefficient of $\sin(\omega_r(t - t_{B0}))$ in (39) equals $\pi I_O/(2H_b)$ or $\pi I_O K_F/2$. Therefore, we have

$$i_{rb}(t) = \frac{\pi K_F}{2}I_O\sin(\omega_r(t - t_{B0})). \tag{42}$$

Below resonance, as shown in Fig. 6, i_{rb} has discontinuity. This creates nonlinearity. In order to obtain the third-order behavioral average equivalent circuit of the *LLC* converter, operating below resonance, the next step is to solve this discontinuity. This can be performed by adjusting the parameters of the *LLC* converter in such a way that the dashed green waveform represents the rectifier current below resonance. The dashed green waveform in Fig. 6 is called the below-resonant equivalent rectifier current (i_{rbe}). In order for this to be correct, the area under i_{rb} from t_{B0} to t_{B2} must be equal to the area under i_{rbe} in the same period of time. This guarantees the transfer of the same energy to the load side in half a switching cycle. The area under i_{rb} from t_{B0} to t_{B2} is called A and calculated as follows:

$$A = \int_{t_{B0}}^{t_{B2}} i_{rb}(t)dt = \int_{t_{B0}}^{t_{B1}} \frac{\pi K_F}{2}I_O\sin(\omega_r(t - t_{B0}))dt. \tag{43}$$

The above equation results in the following:

$$A = \frac{\pi K_F}{2}I_O\frac{1}{\omega_r}[1 - \cos(\pi K_F)]. \tag{44}$$

The area under i_{rb} equals the area under i_{rbe}, in half a switching cycle, only if ω_r and $i_{rb} = n(i_{Lr} - i_{Lm})$ are divided by K_f or alternatively multiplied into H_b. If ω_r is divided by K_f, a new angular frequency, called ω_{rab}, is obtained as follows:

$$\omega_{rab} = \frac{1}{K_f\sqrt{L_rC_r}}. \tag{45}$$

The above process does not change Z_r in (39). Therefore, by using (45), it can be concluded that L_r and C_r are multiplied into K_F. Therefore, the below-resonant equivalent resonant inductance and capacitance can be calculated using the following equations:

$$L_{rab} := K_fL_r \tag{46}$$

$$C_{rab} := K_fC_r. \tag{47}$$

The current through the output capacitor equals $i_{rb} - I_O$. Therefore, the pick-to-pick variation in the output voltage (ΔV_O) of the *LLC* converter, operating below resonance, can be calculated using the following equation:

$$\Delta V_O = \frac{1}{C_O}\int_{t_{B0}}^{t_{B1}}\left(\frac{\pi}{2H_b} - 1\right)I_O\sin(\omega_r(t - t_{B0}))dt - \frac{1}{C_O}\int_{t_{B1}}^{t_{B2}} I_Odt. \tag{48}$$

The result of the above equation is given as follows:

$$\Delta V_O = \frac{1}{C_O}\left(\frac{\pi}{2H_b} - 1\right)\frac{I_O}{\omega_r}\left[1 - \cos\left(\omega_rH_b\frac{T_{\text{sw}}}{2}\right)\right] - \frac{1}{C_O}I_O(1 - H_b)\frac{T_{\text{sw}}}{2}. \tag{49}$$

As discussed, A equals B only if ω_r and i_{rb} are divided by K_f or equivalently multiplied into H_b. Therefore, by applying (45) to the above equation, the following is obtained:

$$\Delta V_O = \frac{H_b}{C_O}\left(\frac{\pi}{2} - 1\right)\frac{2I_O}{\omega_{rb}} - \frac{H_b}{C_O}I_O\frac{T_{\text{sw}}}{2}. \tag{50}$$

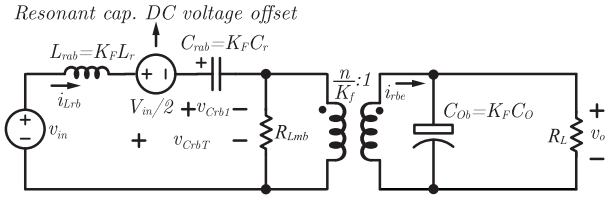

Fig. 7. Below-resonant third-order behavioral average equivalent circuit of the *LLC* converter, in half a switching cycle.

From the above equation, it is clear that the equivalent output capacitance when the *LLC* converter operates below resonance equals C_O/H_b or equivalently $K_f C_O$. Therefore, the below-resonant equivalent output capacitor can be defined as follows:

$$C_{Ob} := K_f C_O = \frac{C_O}{H_b}. \tag{51}$$

All the above discussions result in a third-order behavioral average equivalent circuit, as shown in Fig. 7. This equivalent circuit represents the linear high- and low-frequency steady-state and dynamic behaviors of the *LLC* converter, operating below resonance, in half a switching cycle.

B. Above-Resonant Third-Order Behavioral Average Equivalent Circuit

If it is considered that the *LLC* converter is operating in the steady state and above resonance, according to Fig. 5(a), nV_O drops across the magnetizing inductor L_m from t_{A0} to t_{A2} and causes i_{Lm} to linearly increase. Therefore, the current through the magnetizing inductor can be calculated using the following equation:

$$i_{Lm}(t) = \frac{nV_O}{L_m}(t - t_{A0}) - \frac{\Delta I_{Lma}}{2},\ (t_{A0} < t < t_{A2}). \tag{52}$$

Since $t_{A2} - t_{A0} = T_{\rm sw}/2$, ΔI_{Lma} can be calculated using the following equation:

$$\Delta I_{Lma} = \frac{nV_O}{2L_m F_{\rm sw}}. \tag{53}$$

The average current through the magnetizing inductor of the *LLC* converter, operating above resonance, in half a switching cycle can be calculated using the following equation:

$$\frac{2}{T_{\rm sw}}\int_{t_{A0}}^{t_{A2}} i_{Lm}(t)dt = \frac{2}{T_{\rm sw}}\int_{t_{A0}}^{t_{A2}}\left[\frac{nV_O}{L_m}(t - t_{A0}) - \frac{\Delta I_{Lma}}{2}\right]dt. \tag{54}$$

Solving the above equation reveals that the average current through L_m in half a switching cycle, above resonance, is zero.

The differential equation, describing the above-resonant behavior of the *LLC* converter in Interval I, is given by (2). As shown in Fig. 5(b), $i_{ra} = n(i_{Lr} - i_{Lm})$. By applying this current relationship to (2), the following equation is obtained:

$$V_{\rm in} - nV_O = \frac{L_r}{n}\frac{di_{ra}(t)}{dt} + L_r\frac{di_{Lm}(t)}{dt} + \frac{1}{nC_r}\int_{t_{A0}}^{t} i_{ra}(t)dt + \frac{1}{C_r}\int_{t_{A0}}^{t} i_{Lm}(t)dt + v_{Cr}(t_{A0}). \tag{55}$$

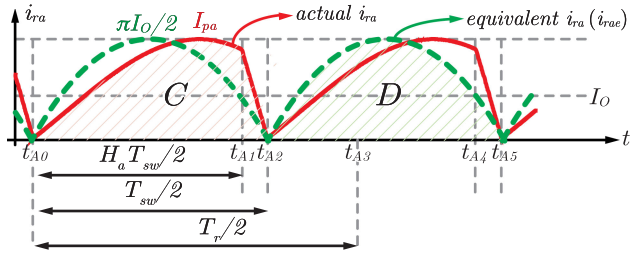

Fig. 8. Actual and equivalent rectifier current of the *LLC* converter, operating above resonance.

By considering the fact that $di_{Lm}/dt = nV_O/L_m$, solving the above equation gives the rectifier current of the *LLC* converter, operating above resonance in Interval I:

$$i_{ra}(t) = \frac{1}{n} \times \frac{V_{\rm in} - v_{Cr}(t_{A0}) - [1 + (L_r/L_m)]nV_O}{Z_r}\sin(\omega_r(t - t_{A0})). \tag{56}$$

In Interval II, the following differential equation describes the dynamic behavior of the *LLC* converter, operating above resonance:

$$-nV_O = \frac{L_r}{n}\frac{di_{ra}(t)}{dt} + L_r\frac{di_{Lm}(t)}{dt} + \frac{1}{nC_r} \times \int_{t_{A1}}^{t} i_{ra}(t)dt + \frac{1}{C_r}\int_{t_{A1}}^{t} i_{Lm}(t)dt + v_{Cr}(t_{A1}). \tag{57}$$

Solving the above equation results in the rectifier current in Interval II

$$i_{ra}(t) = \frac{1}{n}\frac{-v_{Cr}(t_{A1}) - [1 + (L_r/L_m)]nV_O}{Z_r}\sin(\omega_r(t - t_{A1})). \tag{58}$$

By using (56) and (58), the actual waveform of rectifier current is illustrated by red in Fig. 8. As shown in this figure, the load current I_O equals the average of the above-resonant rectifier current in half a switching cycle. Therefore, I_O can be calculated using the following equation:

$$I_O = \frac{2}{T_{\rm sw}}\left[\int_{t_{A0}}^{t_{A1}} I_{pa}\sin(\omega_r(t - t_{A0}))dt + I_{pa}(1 - H_a)\frac{T_{sw}}{2}\sin\left(\omega_r H_a\frac{T_{\rm sw}}{2}\right)\right] \tag{59}$$

where I_{pa} is the pick current of the actual above-resonant rectifier current. By using the above equation, I_{pa} can be calculated as follows:

$$I_{pa} = \frac{I_O}{\frac{1}{K_f\pi}[1 - \cos(K_f H_a\pi)] + \frac{1}{2}(1 - H_a)\sin(K_f H_a\pi)}. \tag{60}$$

According to Fig. 8, the actual rectifier current shows nonlinearity. The above-resonant rectifier current waveform can be modeled by a linear current waveform that guarantees the transfer of the same amount of energy to the output in half a

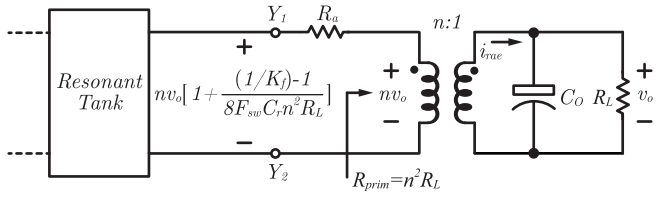

Fig. 9. Circuit seen from the right-hand side port of the resonant tank when the *LLC* converter operates above resonance.

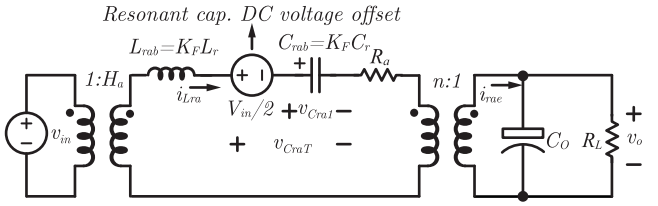

Fig. 10. Above-resonant third-order behavioral average equivalent circuit of the *LLC* converter, in half a switching cycle.

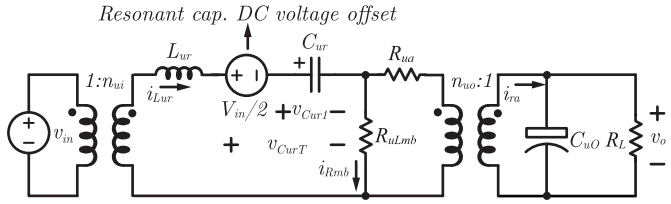

Fig. 11. Unified third-order behavioral average equivalent circuit of the *LLC* converter, in half a switching cycle. This model is valid below, at, and above resonance.

switching cycle. The waveform of the above-resonant equivalent rectifier current (i_{rae}) is shown by green in Fig. 8. As illustrated in this figure, the pick current of the equivalent rectifier current equals $\pi I_O/2$. i_{rae} is an equivalent to i_{ra} if the area under the actual rectifier current (C) equals the area under i_{rae} (D) in half a switching cycle. This condition is satisfied only if ω_r is divided by K_f. In this case, a new angular frequency, called ω_{rab}, already given by (45), is obtained.

Since this equalization does not have any effect on Z_r in (56) and (58), it is concluded that L_r and C_r of the *LLC* converter, operating above resonance, are both multiplied into K_f. The above-resonant equivalent resonant inductance and capacitance can be calculated using (46) and (47), respectively.

The voltage gain of the *LLC* converter, operating above resonance, is given by (25). This equation can be rewritten as follows:

$$V_{\text{in}}(H_a - 0.5) = V_O\left[n + \frac{(1/K_f) - 1}{8nF_{\text{sw}}C_rR_L}\right]. \tag{61}$$

As shown in Fig. 1(a), the resonant tank of the *LLC* converter has two ports. One port is connected to the inverter and another to the rectifier. According to (61), the average voltage applied to the left-hand side port of the resonant tank is $V_{\text{in}}H_a - 0.5V_{\text{in}}$. As discussed in the beginning of Section II, the resonant capacitor of the *LLC* converter has a dc voltage offset of $V_{\text{in}}/2$. Therefore, $V_{\text{in}}H_a - 0.5V_{\text{in}}$ means that the input voltage source is scaled by H_a and then is subtracted by the dc voltage offset of the resonant capacitor. If the average voltage, applied to the right-hand side port of the resonant tank, is shown by V_{Y12}, according to (61), V_{Y12} equals $V_O[n + \frac{(1/K_f)-1}{8nF_{\text{sw}}C_rR_L}]$. By factoring out n, V_{Y12} can be rewritten as follows:

$$V_{Y12} = nV_O\left[1 + \frac{(1/K_f) - 1}{8F_{\text{sw}}C_rn^2R_L}\right]. \tag{62}$$

The above equation explains that nV_O is a fraction of V_{Y12}. Fig. 9 illustrates how nV_O is related to V_{Y12}. As shown in this figure, this relationship can be simply explained by using a resistive voltage divider. In this case, the resistive network is made of the reflected resistor from the secondary to primary side of the transformer (R_{prim}) and a series resistor with the resonant tank, called R_a. By considering (62) and the configuration shown in Fig. 9, R_a can be calculated using the following equation:

$$R_a = \frac{\frac{1}{K_f} - 1}{8F_{\text{sw}}C_r}. \tag{63}$$

All the above discussion results in a third-order behavioral average equivalent circuit that explains the steady-state and high- and low-frequency small-signal dynamic behavior of the *LLC* converter, operating above resonance, in half a switching cycle. This equivalent circuit is shown in Fig. 10.

C. Unified Third-Order Behavioral Average Equivalent Circuit

In this section, the third-order behavioral average equivalent circuits of the *LLC* converter, operating below, at and above resonance are obtained. Instead of working with two equivalent circuits, shown in Figs. 7 and 10, it is more convenient to unify them. The unified third-order behavioral average equivalent circuit of the *LLC* converter valid below, at, and above resonance is shown in Fig. 11. By considering the discussions made in this section and Section II, the parameters of the unified third-order behavioral average equivalent circuit are given as follows:

$$L_{ur} = K_fL_r \tag{64}$$

$$C_{ur} = K_fC_r \tag{65}$$

$$C_{uO} = [K_fu(K_f - 1) + u(1 - K_f)]C_O \tag{66}$$

$$R_{ua} = \frac{(1/K_f) - 1}{8F_{\text{sw}}C_r}u(1 - K_f) \tag{67}$$

$$R_{uLmb} = \frac{4L_mF_r}{K_f - 1}\frac{1}{u(K_f - 1)} \tag{68}$$

$$n_{uo} = \left[\frac{1}{K_f}u(K_f - 1) + u(1 - K_f)\right]n \tag{69}$$

$$n_{ui} = [u(K_f - 1) + H_au(1 - K_f)]n \tag{70}$$

where $u(x)$ is the step function, defined as follows:

$$u(x) = \begin{cases} 1, & x > 0 \\ 0, & x < 0. \end{cases} \tag{71}$$

Depending on the operating region of the *LLC* converter, x can be either $K_f - 1$ or $1 - K_f$.

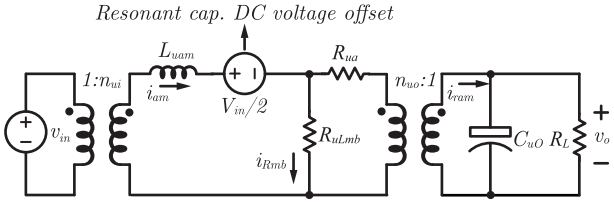

Fig. 12. Unified second-order behavioral average equivalent circuit of the *LLC* converter. This model is valid below, at, and above resonance.

IV. Behavioral Average Equivalent Circuit: Second Stage

For decades, the focus in the *LLC* converter modeling has been reducing the order of the small-signal model while maintaining the accuracy. The key to gaining more simplified small-signal models for the *LLC* converter is to perform the analysis in the time domain. Before, the analysis of *LLC* converters in the time domain was very difficult; however, after the introduction of the homopolarity cycle, the analysis is simplified to a degree that the small-signal dynamic behavior of the *LLC* converter can be expressed by two second-order circuit models.

As discussed, the process of obtaining the ASSM of the *LLC* converter has three stages. The first two stages are involved in the obtainment of two average equivalent circuits, using the behavioral averaging technique. The first stage was addressed in Section III, where the unified third-order behavioral average equivalent circuit of the *LLC* converter below, at, and above resonance was developed. In this section, the analysis is focused on the second stage, in which the unified second-order behavioral average equivalent circuit is obtained. Using this second-order equivalent circuit, two circuit models, representing the small-signal dynamic behavior of the *LLC* converter below, at, and above resonance, are later obtained.

In Section III, the operation of the *LLC* converter below, at, and above resonance was linearized in a half switching cycle, and a unified third-order behavioral average equivalent circuit was developed to illustrate this linear behavior. This equivalent circuit demonstrates both high- and low-frequency average dynamic behaviors of the *LLC* converter. From control point of view, the high-frequency dynamic behavior is not of interest, and linear compensators are designed based on the low-frequency dynamic behavior of a power converter. Generally, linear compensators are designed to achieve a closed-loop bandwidth approximately ten times smaller than the switching frequency of power converters, including *LLC* converters, in order to guarantee a stable closed-loop operation [34]. In most practical applications, having an accurate and straightforward model of the converter up to one-tenth to one-fifth of the switching frequency is enough to design proper compensators. As it will be discussed later in this section, the average response of the *LLC* converter operating in the quiescent area to small changes can be modeled with a second-order system, as shown in Fig. 12. According to the basic concepts governing the electrical circuit theory, the dynamic response of a linear circuit in the steady state, fed by a dc source, can be obtained by analyzing its response to a step input while considering that all the initial conditions are zero from the step input point of view. The output of the *LLC* converter and consequently of the unified third-order equivalent circuit can be connected to any type of load, such as a resistor, current source system, etc.

If a step input v_s with an amplitude of V_S is applied to the third-order behavioral average equivalent circuit in the beginning of a switching cycle, the following differential equation, called ψ_1, can be defined:

$$\psi_1 := -n_{ui}V_S + L_{ur}\frac{di_{Lur}}{dt} + \frac{1}{C_{ur}}\int i_{Lur}dt + R_{uLmb}i_{Rmb} = 0. \quad (72)$$

Since $R_{Lmb}i_{Rmb} = (R_{ua}/n_{uo})i_{ur} + n_{uo}v_O$, the above definition can be rewritten as follows:

$$\psi_1 := -n_{ui}V_S + L_{ur}\frac{di_{Lur}}{dt} + \frac{1}{C_{ur}}\int i_{Lur}dt + R_{ua}\frac{i_{ur}}{n_{uo}} + n_{uo}v_O = 0. \quad (73)$$

The limit of ψ_1 as K_f approaches 1 is given as follows:

$$\lim_{K_f\to 1}\psi_1 := -V_S + L_{ur}\frac{di_{Lur}}{dt} + \left(\frac{1}{C_{ur}} + \frac{n_{uo}^2}{C_{uO}}\right)\int i_{Lur}dt = 0. \quad (74)$$

Since $C_{uO} >> C_{ur}$, the coefficient of the integral in the above equation can be simplified as $1/C_{ur}$. Therefore, solving the above differential equation results in the following equation:

$$i_{Lur} = \frac{V_S}{Z_u}\sin(\omega_u t) \quad (75)$$

where

$$Z_u = \sqrt{\frac{L_{ur}}{C_{ur}}} \quad (76)$$

$$\omega_u = \frac{1}{\sqrt{L_{ur}C_{ur}}}. \quad (77)$$

The average of (75) in its half a switching period is given as follows:

$$\bar{i}_{Lur} = \frac{4V_S C_{ur}}{T_{ur}} \quad (78)$$

where $T_{ur} = 2\pi\sqrt{L_{ur}C_{ur}}$.

If the same step input v_s with an amplitude of V_S is applied to the second-order behavioral average equivalent circuit, shown in Fig. 12, in the beginning of a switching cycle, the following differential equation, called ψ_2, can be defined:

$$\psi_2 := -V_S n_{ui} + L_{uam}\frac{di_{am}}{dt} + R_{ua}(i_{am} - i_{Rmb}) + n_{uo}v_O = 0. \quad (79)$$

The limit of ψ_2 as K_f approaches 1 is given as follows:

$$\lim_{K_f\to 1}\psi_2 := -V_S + L_{uam}\frac{di_{am}}{dt} + \frac{n_{uo}^2}{C_{uO}}\int i_{am}dt = 0. \quad (80)$$

Solving the above differential equation results in the following equation:

$$i_{am} = \frac{V_S}{Z_{am}} \sin(\omega_{am} t) \tag{81}$$

where

$$\omega_{am} = \frac{n_{uo}}{\sqrt{L_{uam} C_{uO}}} \tag{82}$$

$$Z_{am} = n_{uo} \sqrt{\frac{L_{uam}}{C_{uO}}}. \tag{83}$$

By averaging the above equation in half a period of (75), the following equation is obtained:

$$\bar{i}_{am} = \frac{2 V_S C_{uO}}{n_{uo}^2 T_r} \left[1 - cos \left(\pi n_{uo} \sqrt{\frac{L_{ur} C_{ur}}{L_{uam} C_{uO}}} \right) \right]. \tag{84}$$

If the circuit shown in Fig. 12 is a model of the third-order behavioral average equivalent circuit, (78) must be equal with (84). By using this condition, L_{uam} can be calculated using the following equation:

$$L_{uam} = \frac{n_{uo}^2 C_{ur}}{C_{uO}} \frac{\pi^2 L_{ur}}{\left[\cos^{-1} \left(1 - 2 \frac{n_{uo}^2 C_{ur}}{C_{uO}} \right) \right]^2}. \tag{85}$$

V. Average Small-Signal Model

Through the analysis of the homopolarity cycle, two simple second-order circuit models, representing the small-signal dynamic behavior of the *LLC* converter, below, at, and above resonance, can be obtained. The process of obtaining the two circuit models has three stages. So far, the first two stages are covered, and a second-order behavioral average equivalent circuit, demonstrating the low-frequency dynamic behavior of the *LLC* converter, is developed. In this section, the focus of the analysis is on the third stage, in which perturbations are applied to the signals of the *LLC* converter in order to obtain the ASSM of the *LLC* converter below, at, and above resonance.

A. Below-Resonant ASSM

When the *LLC* converter operates below resonance, according to the definition of $u(x)$, provided by (71), $u(1 - K_f) = 0$ and $u(K_f - 1) = 1$. Therefore, according to (64)–(70), the second-order behavioral average equivalent circuit is simplified to the circuit shown in Fig. 13(a). In order to obtain the ASSM of the *LLC* converter, the following perturbations are added to the parameters of the system:

$$f_{\text{sw}} = F_{\text{sw}} + \hat{f}_{\text{sw}} \tag{86}$$

$$v_{\text{in}} = V_{\text{in}} + \hat{v}_{\text{in}} \tag{87}$$

$$v_O = V_O + \hat{v}_O \tag{88}$$

$$i_{am} = I_{am} + \hat{i}_{am}. \tag{89}$$

According to Fig. 13(a), the differential equations, expressing the small-signal dynamic behavior of the *LLC* converter,

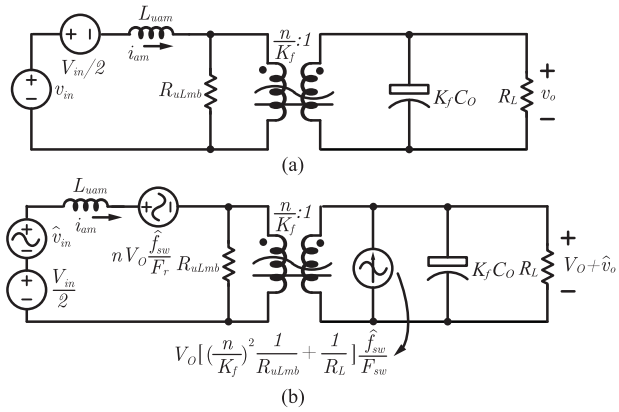

Fig. 13. *LLC* converter, operating below resonance. (a) Second-order behavioral average equivalent circuit. (b) Below-resonant average small-signal circuit model, through which the small-signal transfer function is obtained.

operating below resonance, can be written as follows:

$$\frac{di_{am}}{dt} = \frac{1}{L_{uam}} \left(v_{in} - \frac{V_{\text{in}}}{2} - \frac{n}{K_f} v_O \right) \tag{90}$$

$$\frac{dv_O}{dt} = \frac{1}{K_f C_O} \left\{ \frac{n}{K_f} i_{am} - \left[\left(\frac{n}{K_f} \right)^2 \frac{1}{R_{uLmb}} + \frac{1}{R_L} \right] v_O \right\}. \tag{91}$$

By applying the perturbations given by (86)–(89) to (90) and (91), neglecting the second-order perturbations, and considering that $I_{am} = (K_f/n)(V_O/R_L) + (n/K_f)(V_O/R_{uLmb})$ and $K_f = F_r/F_{\text{sw}}$, the following equations are obtained:

$$\frac{d\hat{i}_{am}}{dt} = \frac{1}{L_{uam}} \left[\frac{V_{\text{in}}}{2} + \hat{v}_{\text{in}} - \frac{n}{K_f} (V_O + \hat{v}_O) - \frac{n V_O}{F_r} \hat{f}_{\text{sw}} \right] \tag{92}$$

$$\frac{d\hat{v}_O}{dt} = \frac{1}{K_f C_O} \left\{ \frac{n}{K_f} (I_{am} + \hat{i}_{am}) - \left[\left(\frac{n}{K_f} \right)^2 \frac{1}{R_{uLmb}} + \frac{1}{R_L} \right] (V_O + \hat{v}_O) + \left[\left(\frac{n}{K_f} \right)^2 \frac{1}{R_{uLmb}} + \frac{1}{R_L} \right] V_O \frac{\hat{f}_{\text{sw}}}{F_{\text{sw}}} \right\}. \tag{93}$$

The above equations describe the ASSM of the *LLC* converter, operating below resonance, and can be translated to the circuit shown in Fig. 13(b).

By using the circuit representation of the below-resonant ASSM, shown in Fig. 13(b), the control-to-output and input-to-output transfer functions are given as follows:

$$\frac{\hat{v}_o}{\hat{f}_{\text{sw}}} = \frac{\frac{K_{2b} K_f}{n} L_{uam} S - K_{1b}}{\frac{K_f}{n} L_{uam} S \left[S K_f C_O + \frac{1}{R_L} + \left(\frac{n}{K_f} \right)^2 \frac{1}{R_{uLmb}} \right] + \frac{n}{K_f}} \tag{94}$$

$$\frac{\hat{v}_o}{\hat{v}_{\text{in}}} = \frac{1}{\frac{K_f}{n} L_{uam} S \left[S K_f C_O + \frac{1}{R_L} + \left(\frac{n}{K_f} \right)^2 \frac{1}{R_{uLmb}} \right] + \frac{n}{K_f}} \tag{95}$$

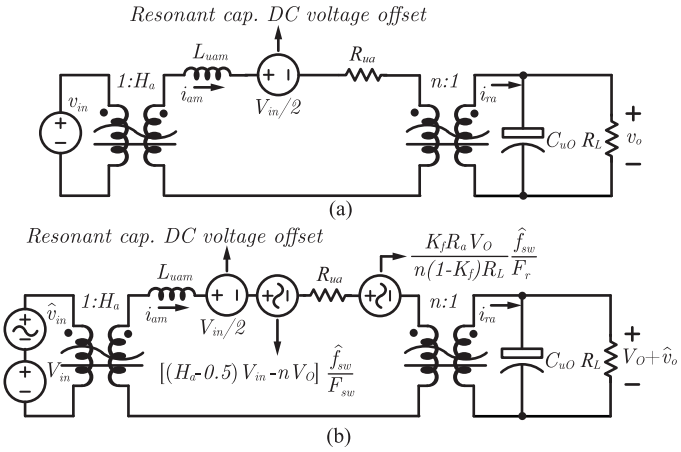

Fig. 14. *LLC* converter, operating above resonance. (a) Second-order behavioral average equivalent circuit. (b) Above-resonant average small-signal circuit model, through which the small-signal transfer function is obtained.

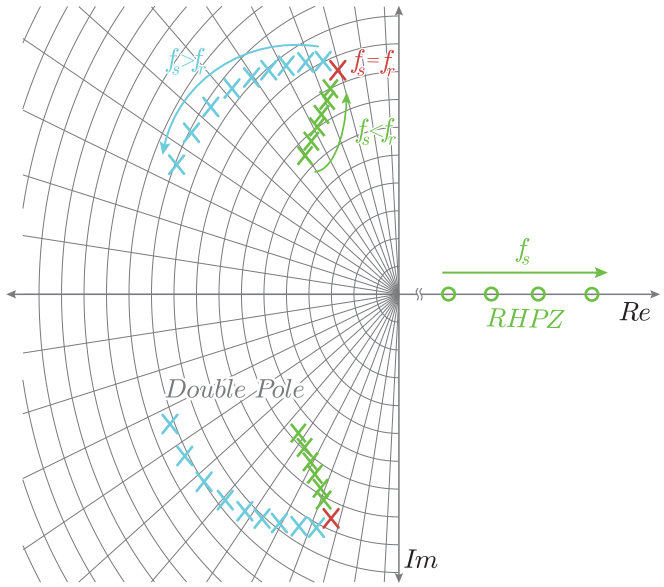

Fig. 15. Pole and zero displacement of the below- and above-resonant small-signal transfer functions.

where

$$K_{1b} = \frac{nV_O}{F_r} \tag{96}$$

$$K_{2b} = \left[\left(\frac{n}{K_f}\right)^2 \frac{1}{R_{uLmb}} + \frac{1}{R_L}\right]\frac{V_O}{F_{\text{sw}}}. \tag{97}$$

B. Above-Resonant ASSM

When the *LLC* converter operates above resonance, according to the definition of $u(x)$, provided by (71), $u(1-K_f)=1$ and $u(K_f-1)=0$. Therefore, according to (64)–(70), the second-order behavioral average equivalent circuit is simplified to the circuit shown in Fig. 14(a). In order to obtain the ASSM of the *LLC* converter, the perturbations given by (86)–(89) are added to the signals of the converter.

According to Fig. 14(a), the differential equations, expressing the small-signal dynamic behavior of the *LLC* converter, operating above resonance, can be written as follows:

$$\frac{di_{am}}{dt} = \frac{1}{L_{uam}}\left(H_a v_{\text{in}} - \frac{V_{\text{in}}}{2} - R_{ua}i_{am} - nv_O\right) \tag{98}$$

$$\frac{dv_O}{dt} = \frac{1}{C_{uO}}\left(ni_{am} - \frac{1}{R_L}v_O\right). \tag{99}$$

By applying the perturbations given by (86)–(89) to (98) and (99), neglecting the second-order perturbations, and considering that $I_{am} = (1/n)(V_O/R_L)$ and $K_f = F_r/F_{\text{sw}}$, the following equations are obtained:

$$\frac{d\hat{i}_{am}}{dt} = \frac{1}{L_{uam}}\left[H_a(V_{\text{in}}+\hat{v}_{\text{in}}) - \frac{V_{\text{in}}}{2} - \left[\left(H_a - \frac{1}{2}\right)V_{\text{in}} - nV_O\right]\frac{\hat{f}_{\text{sw}}}{F_{\text{sw}}} - R_{ua}(\hat{i}_{am}+I_{am}) - \frac{K_f R_{ua}V_O}{n(1-K_f)R_L}\frac{\hat{f}_{\text{sw}}}{F_r} - n(V_O+\hat{v}_o)\right] \tag{100}$$

$$\frac{d\hat{v}_O}{dt} = \frac{1}{C_{uO}}\left[n(I_{am}+\hat{i}_{am}) - \frac{1}{R_L}(V_O+\hat{v}_O)\right]. \tag{101}$$

The above equations describe the ASSM of the *LLC* converter, operating above resonance, and can be translated to the circuit shown in Fig. 14(b).

By using the circuit representation of the above-resonant ASSM, shown in Fig. 14(b), the control-to-output and input-to-output transfer functions are given as follows:

$$\frac{\hat{v}_o}{\hat{f}_{\text{sw}}} = -\frac{K_{1a}+K_{2a}}{\frac{1}{n}(L_{uam}S+R_{ua})\left(\frac{1}{R_L}+SC_{uO}\right)+n} \tag{102}$$

$$\frac{\hat{v}_o}{\hat{v}_{\text{in}}} = \frac{H_a}{\frac{1}{n}(L_{uam}S+R_{ua})\left(\frac{1}{R_L}+SC_{uO}\right)+n} \tag{103}$$

where

$$K_{1a} = \frac{1}{F_{\text{sw}}}[(H_a-0.5)V_{\text{in}} - nV_O] \tag{104}$$

$$K_{2a} = \frac{K_f R_{ua}V_O}{n(1-K_f)R_L F_r}. \tag{105}$$

The denominators of (94) and (95), and those of (102) and (103), are the same. Moreover, in the control point of view, the control-to-output transfer function is the most important transfer function that linear controllers are often designed based on. Therefore, discussing the poles and zeros of the control-to-output transfer functions suffices. Fig. 15 illustrates the conceptual pole and zero displacements of (94) and (102). The system displays a double pole that moves depending on the switching frequency. As shown in the figure, at different operating points, the system shows different damping ratios and natural frequencies. There is a right-half-plane zero (RHPZ) at below-resonant

TABLE I
SPECIFICATIONS OF THE *LLC* CONVERTER

Parameter	*Value*	*Description*
V_{in}	400 V	Nominal input voltage
V_O	48 V	Nominal output voltage
P_O	650 W	Nominal output power
F_r	96 kHz	Resonant frequency
n	4	Turn ratio of the transformer
L_r	82 μH	Resonant inductor
L_m	240 μH	Magnetizing inductor
C_r	33 nF	Resonant capacitor
C_O	55 μF	Output capacitor

frequency operation. The position of the zero is far from the imaginary axis, and it increases when the switching frequency is increased. Therefore, the effect of the RHPZ in the range of the frequency that a linear controller is designed is not significant and can be neglected.

VI. EXPERIMENTAL AND SIMULATION RESULTS

In order to reduce the complexity of the analysis and to achieve high accuracy in small-signal modeling of the *LLC* converter, below, at, and above resonance, the homopolarity cycle can be introduced to the time-domain equations of the *LLC* converter. The analysis of the homopolarity cycle and average behavior of the converter results in two simple second-order circuit models, which demonstrate the small-signal dynamic behavior of the *LLC* converter. In order to validate the theoretical analyses, in this section, simulation and experimental results of a 650-W *LLC* converter are provided. The specifications of the *LLC* converter are given in Table I.

A. Steady-State Validating Experimental Results

In Section II, the homopolarity cycle concept was defined, and the voltage gain, homopolarity cycle, and switching frequency relationships were obtained. Since the process of obtaining of the ASSM of the *LLC* converter is based on the homopolarity cycle, first, the accuracy of the analysis performed in Section II, especially that of the unified voltage gain equation given by (30) must be validated. In Figs. 16 and 17, the theoretical, simulation, and experimental homopolarity cycle and normalized voltage gain diagrams obtained from the homopolarity cycle and first harmonic approximation (FHA) analysis versus the switching frequency are compared against each other. As shown in these figures, (30) predicts the voltage gain of the *LLC* converter below, at, and above resonance and under different loading conditions with high accuracy. As anticipated, when the switching frequency moves away from F_r, the accuracy of the FHA analysis degrades. In order to plot the FHA voltage gain curves, the equation introduced by [32] is used.

In Fig. 18, the time-domain experimental waveforms of the *LLC* converter, operating below resonance under full- and half-loading conditions, are shown. In this case, the switching frequency equals 80 kHz. As shown in Fig. 18(a) and (b), the period of time during which the polarities of v_{inv} and v_{sec}, in half a switching period, are both the same equals 5.2 μs.

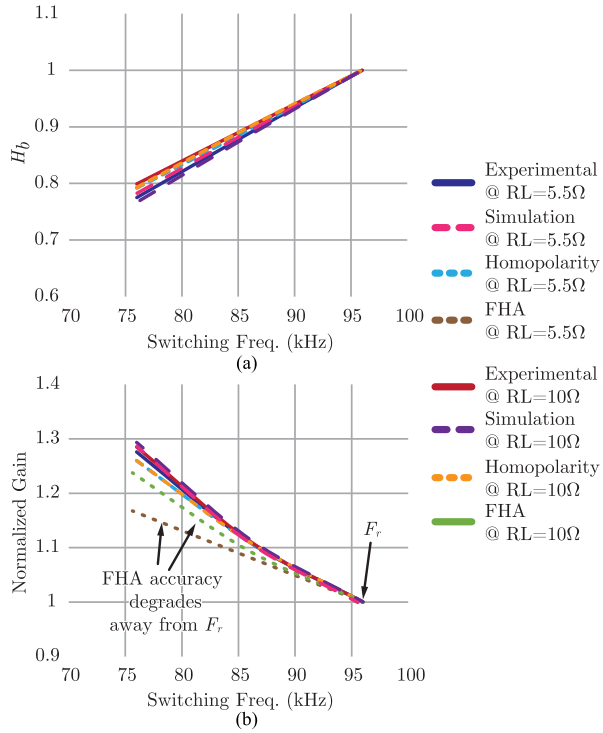

Fig. 16. (a) and (b) theoretical, simulation, and experimental below-resonant normalized gain diagrams. The theoretical curves obtained from the analysis of the homopolarity cycle align well with the experimental and simulation curves. The accuracy of the FHA curves degrades when the switching frequency moves away from the resonant frequency.

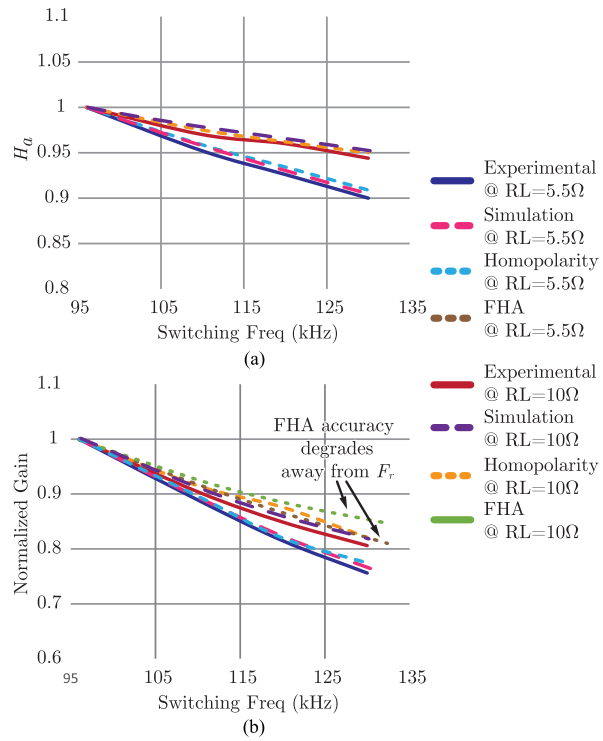

Fig. 17. (a) and (b) theoretical, simulation, and experimental above-resonant normalized gain diagrams. The theoretical curves obtained from the analysis of the homopolarity cycle align well with the experimental and simulation curves. The accuracy of the FHA curves degrades when the switching frequency moves away from the resonant frequency.

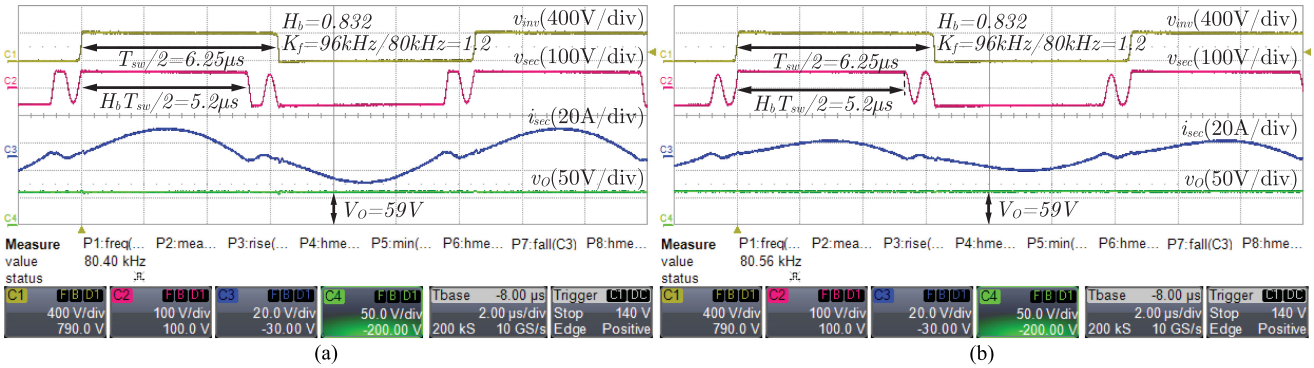

Fig. 18. Below-resonant time-domain experimental waveforms of the *LLC* converter. These waveforms validate the accuracy of the steady-state theoretical analysis. (a) Full-loading condition. (b) Half-loading condition.

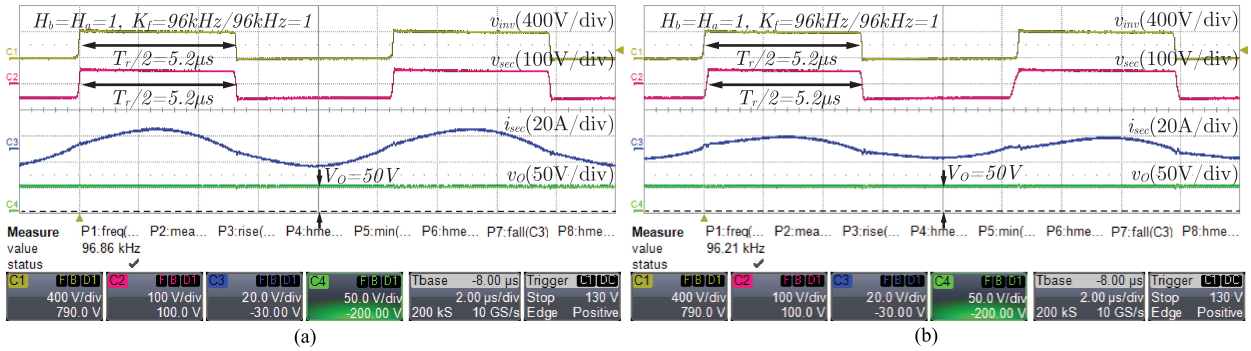

Fig. 19. Resonant time-domain experimental waveforms of the *LLC* converter. These waveforms validate the accuracy of the steady-state theoretical analysis. (a) Full-loading condition. (b) Half-loading condition.

According to the definition of the homopolarity cycle, this time period is $H_bT_{\rm sw}/2$. The resonant frequency of the *LLC* converter is 96 kHz, and therefore, half the resonant period ($T_r/2$) equals 5.2 μs. Therefore, as theoretically predicted in Section II, $H_bT_{\rm sw}/2 = T_r/2$. In Fig. 18(a) and (b), it is also shown that under the full- and half-loading conditions, the output voltage remains the same. According to (12), in this scenario, the output voltage must be equal to 59.5 V. As shown in Fig. 18, the output voltage of the *LLC* converter was measured as 59 V under full- and half-loading conditions. Therefore, the theoretical analysis performed in Section II-A is validated.

In Fig. 19, the time-domain experimental waveforms of the *LLC* converter, operating at resonance under full- and half-loading conditions, are shown. In this case, the switching frequency equals the resonant frequency. As shown in Fig. 19(a) and (b), the period of time during which the polarities of $v_{\rm inv}$ and $v_{\rm sec}$, in half a switching cycle, are both the same equals 5.2 μs. According to the definition of the homopolarity cycle, this time period is $T_{\rm sw}/2$. The resonant frequency of the *LLC* converter is 96 kHz, and therefore, half the resonant period ($T_r/2$) equals 5.2 μs. Therefore, as theoretically predicted in Section II, $T_{\rm sw}/2 = T_r/2$. In Fig. 19(a) and (b), it is also shown that under the full- and half-loading conditions, the output voltage remains the same. According to (18), in this scenario, the output voltage must be equal to 50 V. As shown in Fig. 19, the output voltage of the *LLC* converter was measured as 50 V under full- and half-loading conditions. Therefore, the theoretical analysis performed in Section II-B is validated.

In Fig. 20, the time-domain experimental waveforms of the *LLC* converter, operating above resonance under full- and half-loading conditions, are shown. In this case, the switching frequency equals 120 kHz. As shown in Fig. 20(a), the period of time during which the polarities of $v_{\rm inv}$ and $v_{\rm sec}$, in half a switching cycle, are both the same equals 3.85 μs. According to the definition of the homopolarity cycle, this time period is $H_aT_{\rm sw}/2$. The voltage gain of the *LLC* converter can be theoretically calculated using (25). According to (25), the output voltage of the converter under the full-loading condition must be 40 V. The output voltage of the *LLC* converter under the full-loading condition was measured 40 V. As shown in Fig. 20(b), the period of time during which the polarities of $v_{\rm inv}$ and $v_{\rm sec}$, in half a switching cycle, are both the same equals 3.95 μs. According to (25), the output voltage of the converter under the half-loading condition must be 42 V. The output voltage of the *LLC* converter under the half-loading condition was measured 42 V. Therefore, the theoretical analysis performed in Section II-C is validated.

B. Frequency-Domain Experimental and Simulation Results

In this article, it was theoretically discussed that the ASSM of the *LLC* converter, below, at, and above resonance, can be obtained by using the homopolarity cycle concept and through

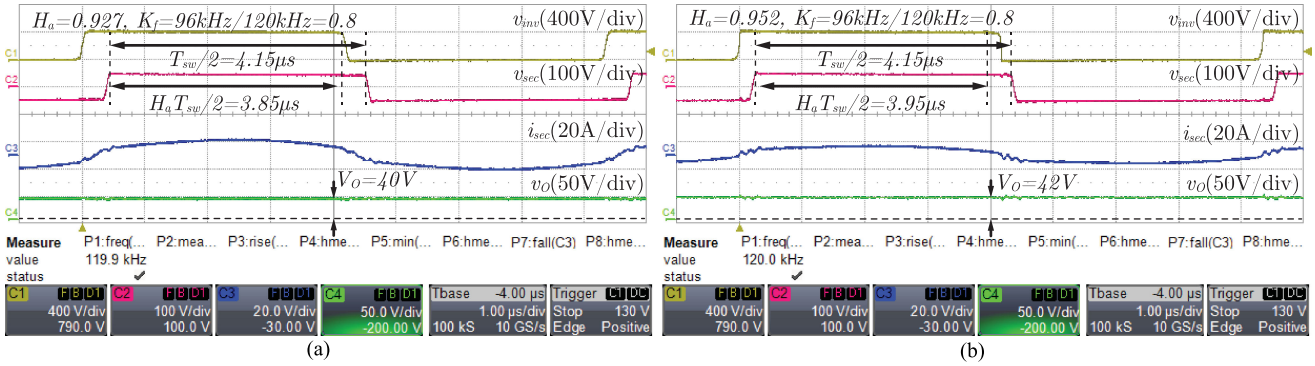

Fig. 20. Above-resonant time-domain experimental waveforms of the *LLC* converter. These waveforms validate the accuracy of the steady-state theoretical analysis. (a) Full-loading condition. (b) Half-loading condition.

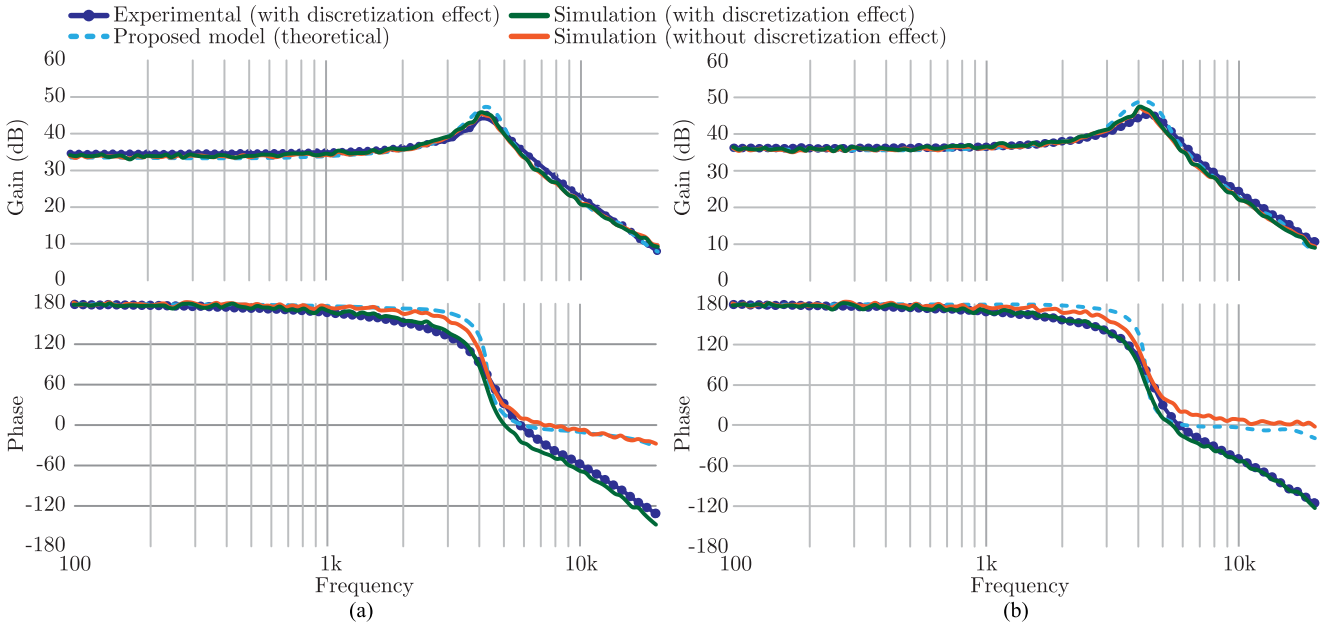

Fig. 21. Below-resonant experimental, simulation, and theoretical Bode diagrams of the proposed small-signal model and *LLC* converter. These Bode diagrams validate the accuracy of the theoretical dynamic analysis, with and without the discretization and time-delay effects: (a) under 5.5-Ω resistive load and (b) under 10-Ω resistive load. The discretization and time-delay effects are due to the digital implementation of the modulation system.

a three-stage process. All the theoretical analyses have resulted in two circuit models, shown in Figs. 13 and 14. These circuit models describe the small-signal dynamic behavior of the *LLC* converter below, at, and above resonance. In order to validate the accuracy of the proposed ASSMs and their relative transfer functions, the Bode diagram analysis, under different frequency and loading conditions, is required. This is performed by using an experimental setup and a simulation software.

In Figs. 21–23, the comparative theoretical, simulation, and experimental control-to-output Bode diagrams of the *LLC* converter, operating below, at, and above resonance, under 5.5– and 10-Ω resistive loads are shown. In these figures, the dashed light blue, orange, dark green, and dark blue diagrams represent the Bode diagrams of the proposed ASSM (theoretical), simulated *LLC* converter without the discretization effect, simulated ASSM with the discretization effect, and experimentally implemented *LLC* converter with discretization effect, respectively. The discretization and time-delay effects happen when the modulation system of a converter is digitally implemented. In the *LLC* converter, experimentally implemented, the TMS320F2835 DSP is used to generate the control signal, which is the switching frequency. In order to apply the perturbation and perform the Bode diagram analysis, the frequency analyzer Venable Model 3120 is used. The perturbing signal, generated by the frequency analyzer, is applied to the analog-to-digital converter (ADC) of the DSP. In order to keep the experimental tests reliable, the sampling time of the DSP ADC is synchronized with the control signal. Therefore, two phenomena happens: discretization and time delay. Discretization occurs due the fact that the ADC is indeed a sample-and-hold system and converts an analog signal to a discrete one. The time-delay effect is seen because the ADC is synchronized with the control signal.

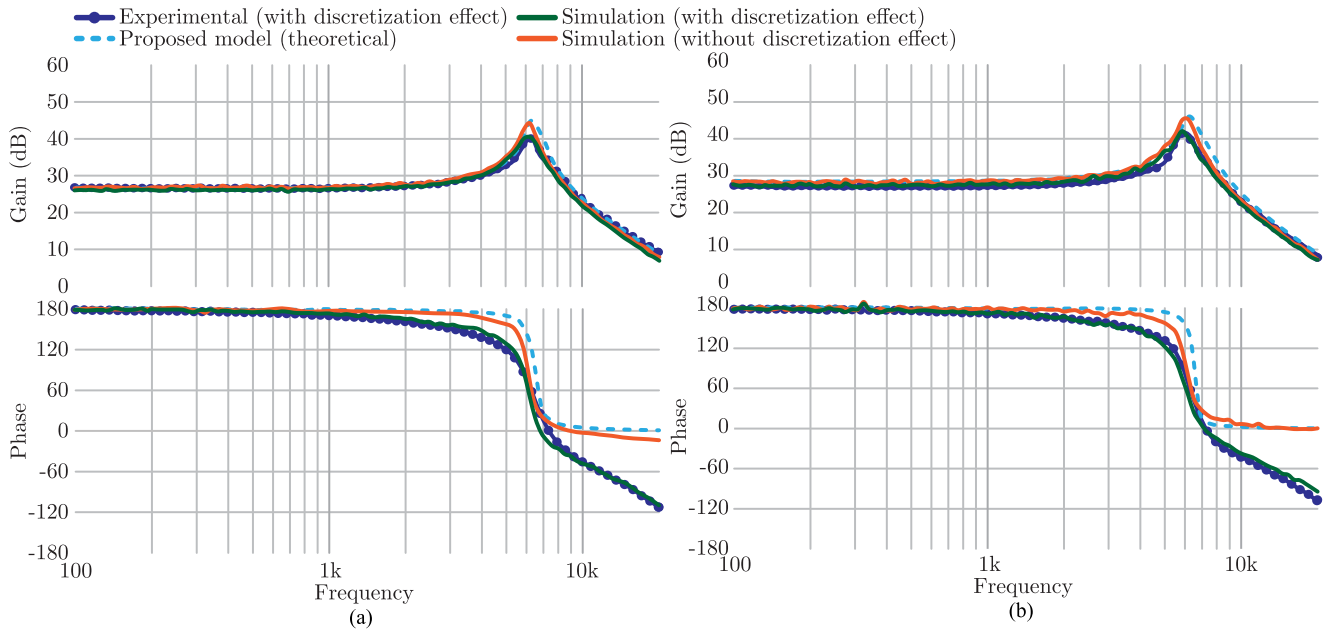

Fig. 22. Resonant experimental, simulation, and theoretical Bode diagrams of the proposed small-signal model and *LLC* converter. These Bode diagrams validate the accuracy of the theoretical dynamic analysis, with and without the discretization and time-delay effects: (a) under 5.5-Ω resistive load and (b) under 10-Ω resistive load. The discretization and time-delay effects are due to the digital implementation of the modulation system.

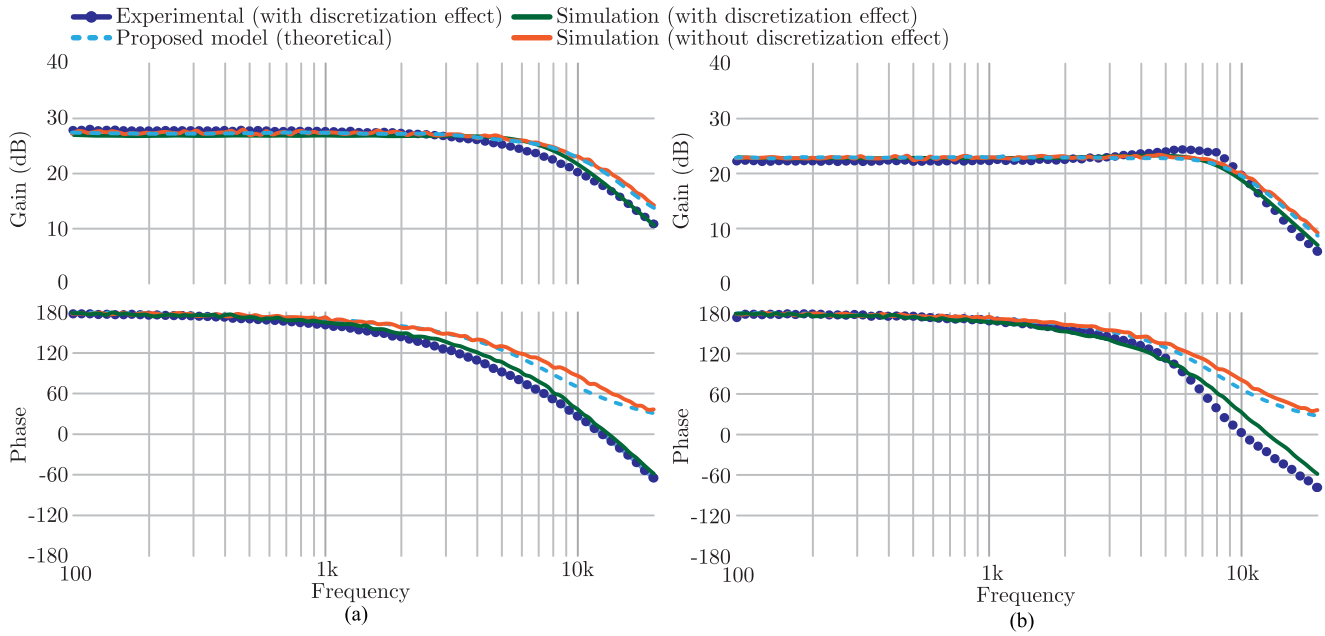

Fig. 23. Above-resonant experimental, simulation, and theoretical Bode diagrams of the proposed small-signal model and *LLC* converter. These Bode diagrams validate the accuracy of the theoretical dynamic analysis, with and without the discretization and time-delay effects: (a) under 5.5-Ω resistive load and (b) under 10-Ω resistive load. The discretization and time-delay effects are due to the digital implementation of the modulation system.

This means that at the beginning of every switching cycle, the ADC starts the conversion, and also, the switching frequency of the control-signal is updated. Since at the beginning of a switching cycle, the ADC just starts the converting process, the control signal is updated with the last switching frequency value remained in the memory of the ADC. Therefore, a time delay equal to the period of a switching cycle (T_{sw}) is created. Looking at the comparative Bode diagrams shown in Figs. 21–23, it is evident that the proposed ASSM accurately predicts the small-signal dynamic behavior of the *LLC* converter, operating below, at, and above resonance and under different loading conditions. As expected, the discretization and time-delay effects can be seen in the experimental Bode diagrams. If the effects of discretization and time delay are considered in the theoretical

control-to-out transfer functions, the dark green diagrams in Figs. 21–23 are obtained. These diagrams are identical to their relative experimental Bode diagrams.

As earlier mentioned, this article mainly focuses on characterizing the *LLC* converter low-frequency small-signal dynamic behavior. The reason of this approach is that accurate small-signal models are desired for the design and implementation of linear compensators. If the compensator gain at the switching frequency is too large, then these switching harmonics are amplified by the compensator and can disrupt the operation of the frequency modulator. Therefore, the compensator network should contain poles at a frequency less than the switching frequency. This consideration typically restricts the crossover frequency to be less than approximately 10% of the converter switching frequency [34]. As a result, in most practical applications, having an accurate and straightforward model of the converter up to one-tenth to one-fifth of the switching frequency is enough to design proper compensators.

As shown in Figs. 21 and 22, the accuracy of the proposed small-signal circuit models is validated at a frequency 20 kHz, which is sufficient for designing linear compensators. 20 kHz is one-fifth of the resonant frequency (96 kHz). Therefore, the proposed second-order circuit models are accurate enough in the range of interest.

VII. Conclusion

Due to the complexity, small-signal modeling for *LLC* converters has been traditionally performed using empirical/simulation methods (yielding limited insight into the dynamic behavior) or in the vicinity of the resonant frequency (suffering from low accuracy below and above resonance). In this article, a new average small-signal modeling technique, based on the homopolarity cycle concept, for *LLC* converters was proposed. The analysis of the homopolarity cycle in the time domain showed that high accuracy, low complexity, and small-signal circuit representation from below- to above-resonant operations can all be achieved when deriving the small-signal model of *LLC* converters. It was also shown that no simulation, numerical computing, or programming software packages are required to obtain the proposed average small-signal circuit models and their small-signal transfer functions. In order to validate the theoretical analyses, a 650-W *LLC* converter was practically implemented. Both the steady-state and dynamic operations were justified through experimental and simulation results. The results showed that the proposed circuit models predict the small-signal dynamic behavior of the *LLC* converter with high accuracy from below- to above-resonant operations.

References

[1] H. Haga and F. Kurokawa, "Modulation method of a full-bridge three-level LLC resonant converter for battery charger of electrical vehicles," *IEEE Trans. Power Electron.*, vol. 32, no. 4, pp. 2498–2507, Apr. 2017.

[2] J. Y. Lee, Y. S. Jeong, and B. M. Han, "An isolated DC/DC converter using high-frequency unregulated LLC resonant converter for fuel cell applications," *IEEE Trans. Ind. Electron.*, vol. 58, no. 7, pp. 2926–2934, Jul. 2011.

[3] M. Shang, H. Wang, and Q. Cao, "Reconfigurable LLC topology with squeezed frequency span for high-voltage bus-based photovoltaic systems," *IEEE Trans. Power Electron.*, vol. 33, no. 5, pp. 3688–3692, May 2018.

[4] I. Demirel and B. Erkmen, "A very low-profile dual output LLC resonant converter for LCD/LED TV applications," *IEEE Trans. Power Electron.*, vol. 29, no. 7, pp. 3514–3524, Jul. 2014.

[5] M. Mohammadi and M. Ordonez, "Extreme start-up response of LLC converters using average geometric control," in *Proc. IEEE Energy Convers. Congr. Expo.*, Milwaukee, WI, USA, pp. 1–7, 2016.

[6] G. W. Wester and R. D. Middlebrook, "Low-frequency characterization of switched DC-DC converters," *IEEE Trans. Aerosp. Electron. Syst.*, vol. AES-9, no. 3, pp. 376–385, May 1973.

[7] G. Pavlov, A. Obrubov, and I. Vinnichenko, "The linearized dynamic model of the series resonant converter for small signals," in *Proc. 2nd Int. Conf. Intell. Energy Power Syst.*, Kiev, Ukraine, 2016, pp. 1–5.

[8] I. Batarseh, C. Megalemos, and M. Sznaier, "Small signal analysis of the LCC-type parallel resonant converter," *IEEE Trans. Aerosp. Electron. Syst.*, vol. 32, no. 2, pp. 702–713, Apr. 1996.

[9] V. Agarwal and A. K. S. Bhat, "Small signal analysis of the LCC-type parallel resonant converter using discrete time domain modeling," *IEEE Trans. Ind. Electron.*, vol. 42, no. 6, pp. 604–614, Dec. 1995.

[10] T. G. Subhash Joshi and V. John, "Small signal audio susceptibility model for series resonant converter," in *Proc. IEEE Int. Conf. Power Electron., Drives Energy Syst.*, Trivandrum, India, 2016, pp. 1–6.

[11] J. Stahl, H. Steuer, and T. Duerbaum, "Discrete modeling of resonant converters—Steady state and small signal description," in *Proc. IEEE Energy Convers. Congr. Expo.*, Raleigh, NC, USA, pp. 1578–1584, 2012.

[12] A. J. Forsyth, Y. K. E. Ho, and H. M. Ong, "Comparison of small-signal modelling techniques for the series-parallel resonant converter," in *Proc. Int. Conf. Power Electron. Variable-Speed Drives*, London, U.K., 1994, pp. 268–273.

[13] R. J. King and T. A. Stuart, "Small-signal model for the series resonant converter," *IEEE Trans. Aerosp. Electron. Syst.*, vol. AES-21, no. 3, pp. 301–319, May 1985.

[14] M. F. Menke, A. R. Seidel, and R. V. Tambara, "LLC LED driver small-signal modeling and digital control design for active ripple compensation," *IEEE Trans. Ind. Electron.*, vol. 66, no. 1, pp. 387–396, Jan. 2019.

[15] A. Tahavorgar and J. E. Quaicoe, "Stability and small signal analysis of the dual series-resonant DC-DC converter," *IEEE Trans. Power Electron.*, vol. 34, no 2, pp. 1420–1430, Feb. 2019.

[16] S. Tian, F. C. Lee, and Q. Li, "A simplified equivalent circuit model of series resonant converter," *IEEE Trans. Power Electron.*, vol. 31, no. 5, pp. 3922–3931, May 2016.

[17] C. Buccella, C. Cecati, H. Latafat, P. Pepe, and K. Razi, "Linearization of LLC resonant converter model based on extended describing function concept," in *Proc. IEEE Int. Workshop Intell. Energy Syst.*, Vienna, Austria, 2013, pp. 131–136.

[18] C. Chang, E. Chang, C. Cheng, H. Cheng, and S. Lin, "Small signal modeling of LLC resonant converters based on extended describing function," in *Proc. Int. Symp. Comput., Consum. Control*, Taichung, Taiwan, 2012, pp. 365–368.

[19] E. X. Yang, F. C. Lee, and M. M. Jovanovic, "Small-signal modeling of series and parallel resonant converters," in *Proc. IEEE Appl. Power Electron. Conf. Expo.*, Boston, MA, USA, 1992, pp. 785–792.

[20] W. Dai, "Modeling and efficiency-based control of interleaved LLC converters for PV DC microgrid," in *Proc. IEEE Ind. Appl. Soc. Annu. Meeting*, Addison, TX, USA, 2015, pp. 1–8.

[21] S. Tian, F. C. Lee, and Q. Li, "Equivalent circuit modeling of LLC resonant converter," in *Proc. IEEE Appl. Power Electron. Conf. Expo.*, Long Beach, CA, USA, 2016, pp. 1608–1615.

[22] S. Tian, F. C. Lee, Q. Li, and B. Li, "Small-signal equivalent circuit model of series resonant converter," in *Proc. IEEE Energy Convers. Congr. Expo.*, Montreal, QC, Canada, 2015, pp. 172–179.

[23] B. Cheng, F. Musavi, and W. G. Dunford, "Novel small signal modeling and control of an LLC resonant converter," in *Proc. IEEE Appl. Power Electron. Conf. Expo.*, Fort Worth, TX, USA, 2014, pp. 2828–2834.

[24] J.-H. Cheng, A. F. Witulski, and J. L. Vollin, "A small-signal model utilizing amplitude modulation for the class-D converter at fixed frequency," *IEEE Trans. Power Electron.*, vol. 15, no. 6, pp. 1204–1211, Nov. 2000.

[25] G. J. J. van Zyl, "A novel frequency-domain small-signal analysis of resonant power converters," *IEEE Trans. Circuits Syst. I, Reg. Papers*, vol. 51, no. 7, pp. 1379–1384, Jul. 2004.

[26] A. F. Witulski, A. F. Hernandez, and R. W. Erickson, "Small signal equivalent circuit modeling of resonant converters," *IEEE Trans. Power Electron.*, vol. 6, no. 1, pp. 11–27, Jan. 1991.

[27] M. Mohammadi and M. Ordonez, "Fast transient response of series resonant converters using average geometric control," *IEEE Trans. Power Electron.*, vol. 31, no. 9, pp. 6738–6755, Sep. 2016.
[28] M. Mohammadi and M. Ordonez, "Inrush current limit or extreme startup response for LLC converters using average geometric control," *IEEE Trans. Power Electron.*, vol. 33, no. 1, pp. 777–792, Jan. 2018.
[29] Z. Fang, J. Wang, S. Duan, K. Liu, and T. Cai, "Control of an LLC resonant converter using load feedback linearization," *IEEE Trans. Power Electron.*, vol. 33, no. 1, pp. 887–898, Jan. 2018.
[30] F. Degioanni, I. G. Zurbriggen, and M. Ordonez, "Dual-loop controller for LLC resonant converters using an average equivalent model," *IEEE Trans. Power Electron.*, vol. 33, no. 11, pp. 9875–9889, Nov. 2018.
[31] J. Deng, C. C. Mi, R. Ma, and S. Li, "Design of LLC resonant converters based on operation-mode analysis for level two PHEV battery chargers," *IEEE/ASME Trans. Mechatronics*, vol. 20, no. 4, pp. 1595–1606, Aug. 2015.
[32] S. De Simone, *LLC Resonant Half-Bridge Converter Design Guideline*, STMicroelectronics Appl. Note AN2450, Mar. 2014, pp. 1–35.
[33] B. Yang, "Topology investigation for front end DC/DC power conversion for distributed power system," Ph.D. dissertation, Dept. Elect. Eng., Virginia Polytech. Inst. State Univ., Blacksburg, VA, USA, Sep. 2003.
[34] R. W. Erickson and D. Maksimovic, *Fundamentals of Power Electronics*. New York, NY, USA: Springer, 2007, p. 349.

Mehdi Mohammadi (S'14) was born in Isfahan, Iran. He received the M.Sc. degree in electrical engineering (electronics) from the Isfahan University of Technology (IUT), Isfahan, in 2014, and the Ph.D. degree in electrical and computer engineering from the University of British Columbia (UBC), Vancouver, BC, Canada, in 2019.

He is currently with Fortinet Technologies, Burnaby, BC. His research interests include linear/nonlinear controllers, synchronous rectification methods, power delivery network, and soft switching technologies for renewable energy developments and server computer applications.

Dr. Mohammadi received the Best Master of Science Thesis Award in electrical engineering in Iran, awarded by the IEEE Iran section, in 2015, the Superior Master of Science Thesis Award of the IUT in 2015, and the Four Year Fellowship in 2015 and the Graduate Support Initiative Scholarship in 2015 and 2016 from UBC.

Franco Degioanni (S'16) was born in Rio Cuarto, Argentina. He received the Ing. degree in electronics engineering from the National University of Cordoba, Córdoba, Argentina, in 2014, and the M.A.Sc. degree from The University of British Columbia, Vancouver, BC, Canada, in 2018, where he is currently working toward the Ph.D. degree.

His current research interests include the study of modeling techniques and linear and nonlinear strategies for power electronic converters applied to renewable energy systems.

Dr. Degioanni has received numerous awards and scholarships, including a scholarship from the Argentinean Ministry of Science and Technology in 2013, the top #1 Electronic Engineer Award from the National University of Cordoba in 2014, and the Four Year Fellowship from the University of British Columbia in 2018.

Mohammad Mahdavi was born in Isfahan, Iran, in 1984. He received the B.S, M.S., and Ph.D. degrees in electrical engineering from the Isfahan University of Technology, Isfahan, in 2006, 2009, and 2013, respectively.

He joined Islamic Azad University, Isfahan, as an Assistant Professor. He is currently a Postdoctoral Fellow with the Department of Electrical and Computer Engineering, University of British Columbia, Vancouver, BC, Canada. His research interests include power electronics, power factor correction converters, soft-switching techniques, renewable energies, electric vehicles, and high-frequency converters.

Martin Ordonez (S'02–M'09) was born in Neuquen, Argentina. He received the Ing. degree in electronics engineering from the National Technological University, Cordoba, Argentina, in 2003, and the M.Eng. and Ph.D. degrees in electrical engineering from the Memorial University of Newfoundland (MUN), St. John's, NL, Canada, in 2006 and 2009, respectively.

He is currently a Professor and Canada Research Chair in Power Converters for Renewable Energy Systems with the Department of Electrical and Computer Engineering, University of British Columbia (UBC), Vancouver, BC, Canada. He is also the holder of the Fred Kaiser Professorship on Power Conversion and Sustainability at UBC. He was an Adjunct Professor with Simon Fraser University, Burnaby, BC, and MUN. His industrial experience in power conversion includes research and development at Xantrex Technology Inc./Elgar Electronics Corp. (now AMETEK Programmable Power in San Diego, CA, USA). With the support of industrial funds and the Natural Sciences and Engineering Research Council, he has contributed to more than 150 publications and R&D reports.

Dr. Ordonez is a Guest Editor for the IEEE JOURNAL OF EMERGING AND SELECTED TOPICS IN POWER ELECTRONICS, an Associate Editor for the IEEE TRANSACTIONS ON POWER ELECTRONICS, and an Editor for the IEEE TRANSACTIONS ON SUSTAINABLE ENERGY. He serves on several IEEE committees and reviews widely for IEEE/IET journals and international conferences. He received the David Dunsiger Award for Excellence in the Faculty of Engineering and Applied Science in 2009 and the Chancellors Graduate Award/Birks Graduate Medal in 2006. He became a Fellow of the School of Graduate Studies, MUN.